CHAPTER 4

SYNTHESIS AND TRIBOLOGICAL BEHAVIOUR OF MULTI-LAYER GRAPHENE COATINGS

The multi-layer graphene coatings have been synthesised by chemical vapour deposition under the varying conditions of growth temperature, acetylene flow rate, and reaction time. A nickel layer has been electroplated on the bearing steel prior to chemical vapour deposition. The primary focus of this study is to find out the optimum conditions to synthesise multi-layer graphene coatings. This chapter begins with the presentation of results on the characterisation of bearing steel, nickel-plated steel, and multi-layer graphene-coated steel synthesised under different conditions to elicit the optimum conditions. This is followed by the results on the friction and wear behaviour of optimised multi-layer graphene against GCr15 steel ball under both unidirectional and reciprocating sliding. The results have been discussed to understand the effect of growth temperature, gas flow rate, and reaction time on the quality of synthesised graphene. The chapter also includes a detailed discussion on the anti-friction and anti-wear performance of the multi-layer graphene coating on steel and highlights the dominating mechanisms of wear.

4.1 RESULTS

4.1.1 CHEMICAL COMPOSITION OF BEARING STEEL

The chemical composition of the bearing steel, as analysed through energy-dispersive X-ray spectroscopy, has been given in Table 4.1.

Table 4.1 Chemical composition of bearing steel (wt. %).

C	O	Fe	Cr	Ni	Mn	Si
1.20	1.63	93.19	1.81	0.86	0.85	0.46

4.1.2 SURFACE ROUGHNESS OF BEARING STEEL

Figure 4.1 shows the surface topography of the polished GCr15 bearing steel specimen, as examined by a non-contact 3D optical profilometer. It can be observed that the root mean square surface roughness is lower than 20 nm.

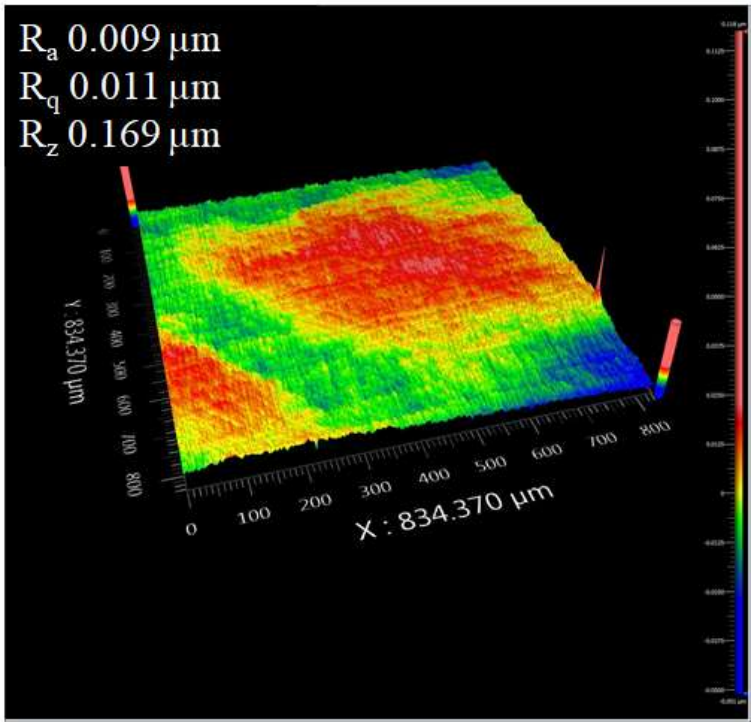

Fig. 4.1 Surface roughness of bearing steel measured by a 3D optical profilometer.

4.1.3 CHARACTERISATION OF ELECTROPLATED NICKEL LAYER

Since the growth of the large area and high-quality graphene is not feasible directly on bearing steel, a nickel layer has been electroplated over the surface of bearing steel prior to graphene deposition to accelerate the graphene growth. The chemical composition of the nickel-plated bearing steel, as analysed through energy-dispersive X-ray spectroscopy, is given in Table 4.2.

Table 4.2 Chemical composition of nickel-plated bearing steel (wt. %).

C	O	Fe	Cr	Ni	Mn	Si
0.74	0.77	0.71	0.36	96.77	0.41	0.24

Surface roughness after nickel electroplating has been measured by a 3D non-contact type profilometer and the same is presented in Fig. 4.2. It can be observed that the root mean square surface roughness is about ~ 35 nm after nickel plating. The thickness of the nickel layer after plating has been measured using scanning electron microscopy, and a micrograph showing the thickness of the plated nickel layer has been presented in Fig. 4.3. It can be observed that the thickness of the plated nickel layer over the bearing steel is ~ 25 μm.

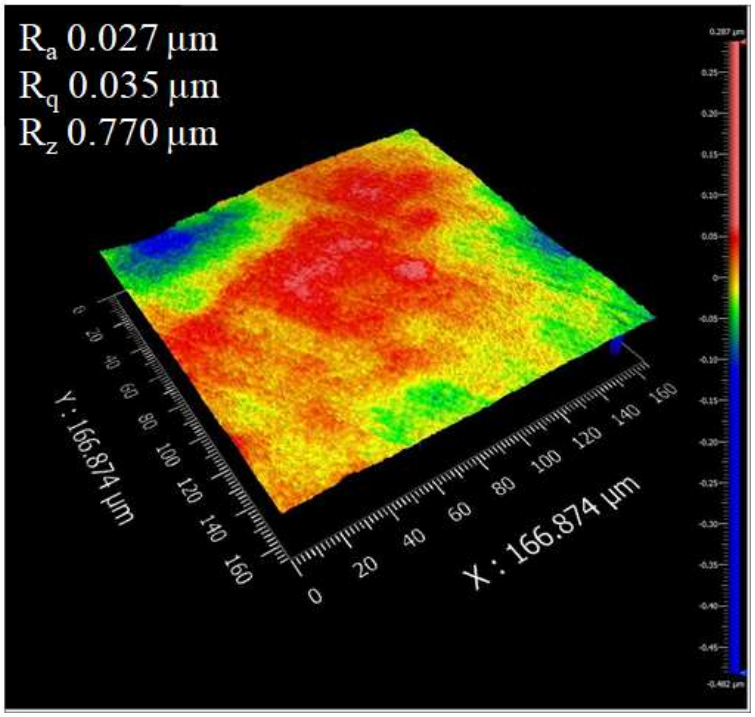

Fig. 4.2 Surface roughness of nickel-plated steel measured by a 3D optical profilometer.

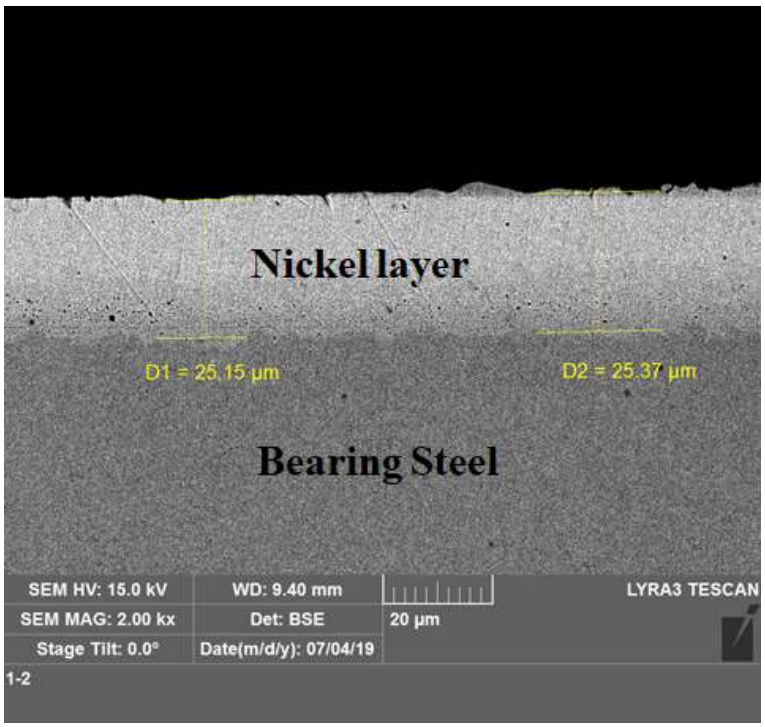

Fig. 4.3 Cross-sectional SEM micrograph showing the thickness of the nickel layer after electroplating.

4.1.4 CHARACTERISATION OF GRAPHENE FILMS

4.1.4.1 Effect of Temperature on Growth of CVD Graphene

The temperature is the crucial parameter for the growth of high-quality graphene, and hence, the effect of growth temperature on the synthesis of graphene has been investigated. The growth temperature has been varied between 650 ℃ and 950 ℃ (in the interval of 100 ℃) while keeping a fixed reaction time of 20 min and an acetylene flow rate of 6 sccm. Figure 4.4 presents the optical micrographs of graphene synthesised at different temperatures of 650, 750, 850, and 950 ℃. We have selected the most occurred region in each surface as a representative micro-image of graphene grown at different growth temperatures. From the figure, it can be observed that the graphene is synthesised in the form of patches with varying thicknesses.

Figure 4.5 represents the Raman spectra of graphene grown on surfaces at different growth temperatures, which shows the presence of D, G, and 2D peak mainly for each growth temperature, at ~ 1350 cm^{-1}, ~ 1580 cm^{-1}, and ~ 2700 cm^{-1}, respectively. However, two more peaks at ~ 2460 cm^{-1} (G^{*}) and ~ 2944 cm^{-1} (D+D') could also be seen in Fig. 4.5. Although the steel specimen with pre-plated nickel exhibits a Raman signal indicative of the presence of graphene at every temperature, the sharpest D peak has been observed for a growth temperature of 650 ℃. One may observe a decrease in D peak intensity with an increase in growth temperature to 750 ℃. However, D peak has been found to be almost absent at the growth temperatures of 850 and 950 ℃, as evident from Fig. 4.5.

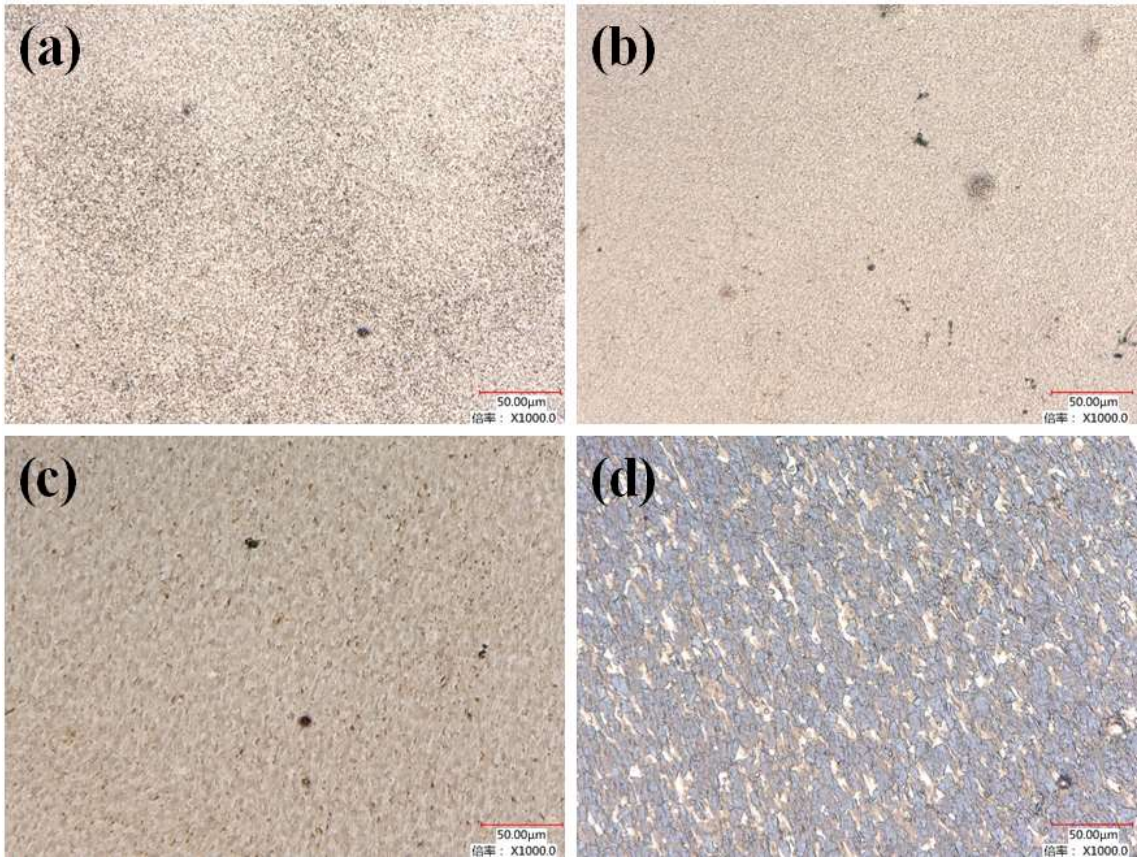

Fig. 4.4 Optical images of CVD-grown graphene for various growth temperatures: (a) 650 °C, (b) 750 °C, (c) 850 °C, and (d) 950 °C under a gas mixture of 6 sccm C_2H_2 and 20 sccm H_2 for 20 min.

Figure 4.6 presents the I_D/I_G and I_{2D}/I_G ratios for graphene growth at different growth temperatures, as obtained from Fig. 4.5. The I_D/I_G ratios for the graphene grown at 650, 750, 850, and 950 °C have been found to be 1.56, 1.12, 0.04, and 0.06, respectively. The ratios of I_D/I_G have been observed to decrease with increasing temperature up to 850 °C, and no significant change in I_D/I_G ratio could be observed beyond that. The I_{2D}/I_G ratios for the graphene grown at 650, 750, 850, and 950 °C have been found to be 0.36, 0.42, 0.58, and 0.44, respectively. The ratio has been observed to increase with increasing temperature from 650 to 850 °C. However, a reduction in I_{2D}/I_G ratio occurs with an increase in temperature from 850 to 950 °C, indicating that a maximum I_{2D}/I_G ratio has occurred for a growth temperature of 850 °C. Hence, As I_{2D}/I_G

value ~ 1 is the representative of bilayer graphene, the I_{2D}/I_G ratios present that the steel surface is covered by multi-layer graphene. Since the lowest I_D/I_G and the highest I_{2D}/I_G have been observed for a growth temperature of 850 °C, this temperature is selected as the optimum temperature to study further the effect of acetylene flow rate and reaction time which is described in the next section.

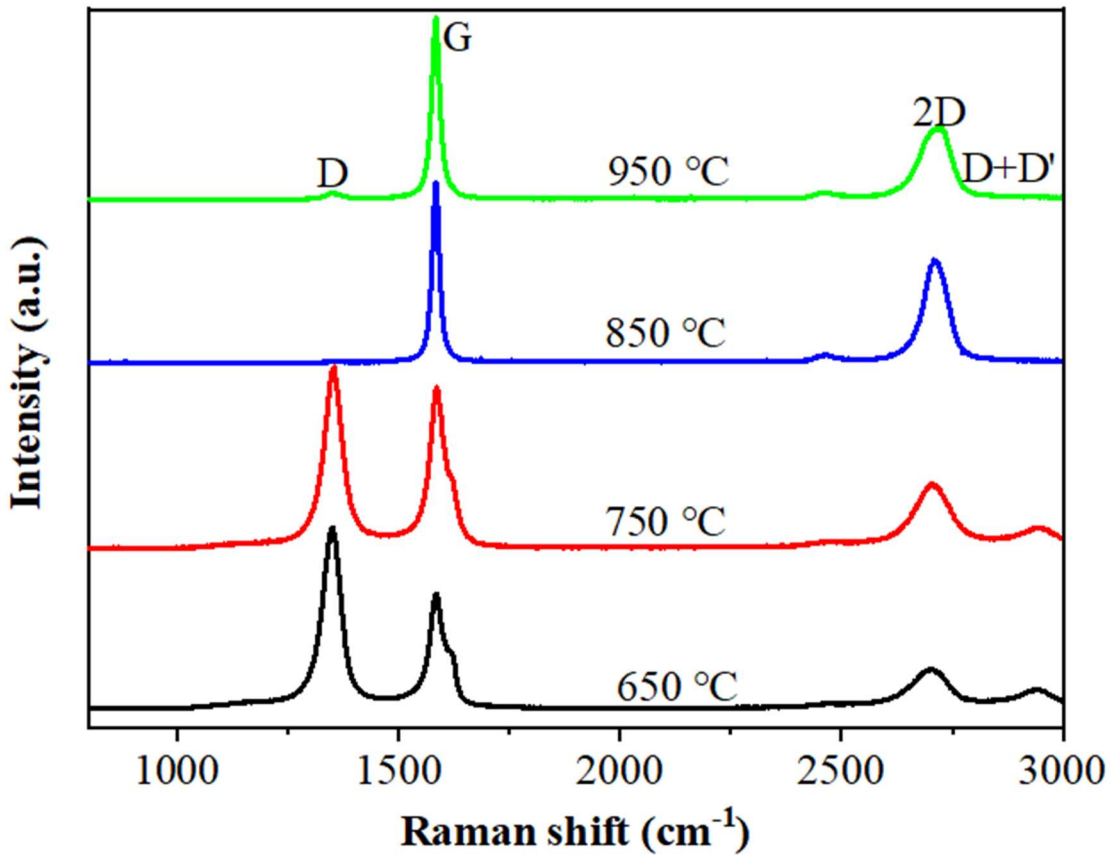

Fig. 4.5 Raman spectra of graphene grown on nickel-plated bearing steel at various growth temperatures under a gas mixture of 6 sccm C_2H_2 and 20 sccm H_2 for 20 min.

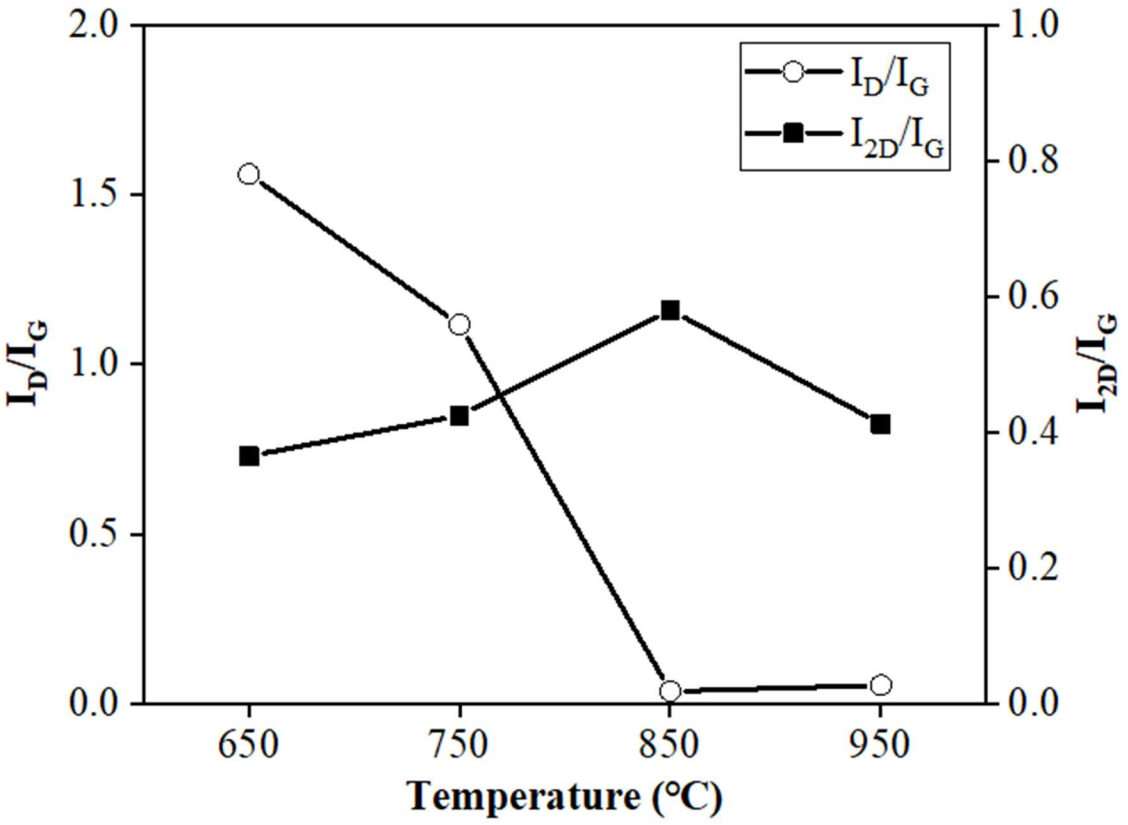

Fig. 4.6 The ratios of I_D/I_G and I_{2D}/I_G of graphene grown on nickel-plated steel at various growth temperatures under a gas mixture of 6 sccm C_2H_2 and 20 sccm H_2 for 20 min.

4.1.4.2 Effect of Acetylene Flow Rate on Growth of CVD Graphene

Another important parameter, which affects the quality of grown graphene significantly is the flow rate of hydrocarbon. In order to understand the influence of acetylene flow rate on the growth of graphene on nickel-plated steel, the flow rate of acetylene has been varied during the reaction stage to synthesise the graphene while keeping the H_2 flow rate constant. The effect of the acetylene flow rate has been studied for three different flow rates, i.e., 6, 8, and 10 sccm. Figures 4.4 (c) and 4.7 (a and b) show the optical micrographs of graphene synthesised respectively, for 6, 8, and 10 sccm flow rates of acetylene. Figure 4.8 shows the Raman spectra of graphene grown with different acetylene flow rates of 6, 8, and 10 sccm. The position of 2D peak has been

found to shift from 2709 cm^{-1} (6 sccm) to 2714 cm^{-1} (8 sccm) and 2719 cm^{-1} (10 sccm) with increasing flow rate of acetylene, as seen from Fig. 4.8. Further, one may also observe the suppression of 2D and G peak intensities and strengthening of D peak with increase in acetylene flow rate.

Figure 4.9 shows the peak intensity ratios (I_D/I_G and I_{2D}/I_G) for different acetylene flow rates. I_{2D}/I_G ratios are found to be 0.58, 0.37, and 0.28, respectively, corresponding to acetylene flow rates of 6, 8, and 10 sccm, while I_D/I_G is found to remain under 0.05 for each flow rate. One may infer that the I_{2D}/I_G ratio is maximum and I_D/I_G is minimum for 6 sccm flow rate among all the flow rates used in the study, hence the flow rate of 6 sccm has been selected as the optimum flow rate to study further the effect of reaction time at the optimised growth temperature (i.e., 850 ℃).

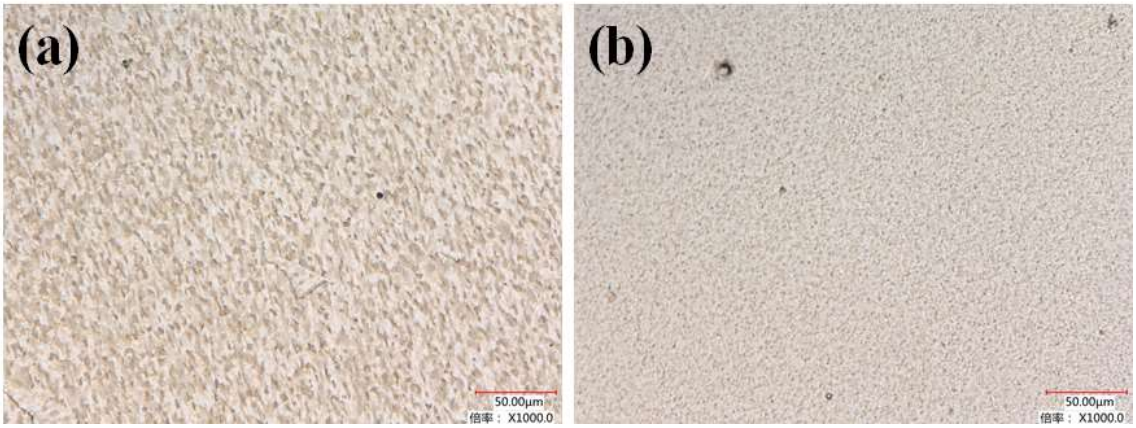

Fig. 4.7 Optical images of CVD-grown graphene for growth temperatures of 850 ℃ under various gas mixture of (a) 8 sccm, (b) 10 sccm C_2H_2, and 20 sccm H_2 for 20 min.

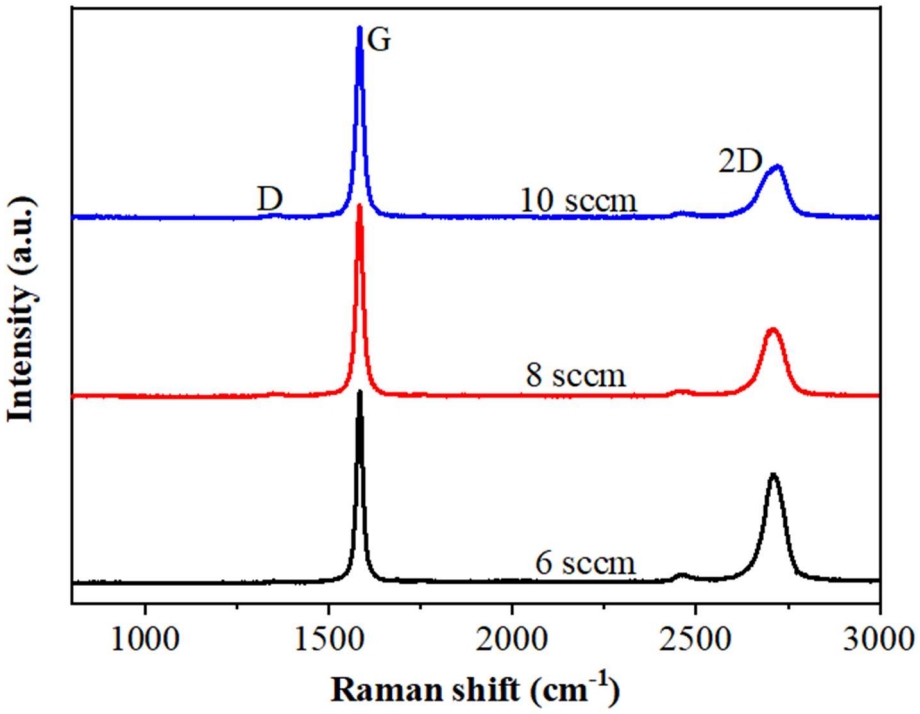

Fig. 4.8 Raman spectra of graphene grown on nickel-plated steel for various acetylene flow rates at 850 ℃ growth temperature and 20 min reaction time.

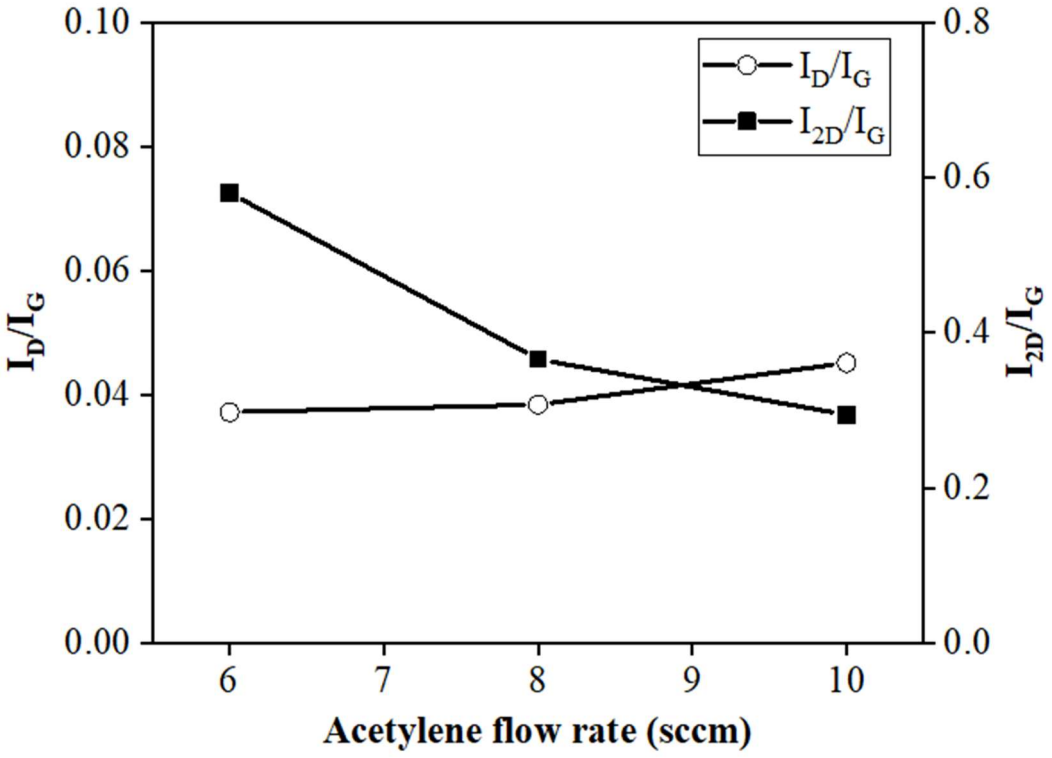

Fig. 4.9 The ratios of I_D/I_G and I_{2D}/I_G of graphene grown on nickel-plated steel for various acetylene flow rates at 850 ℃ growth temperature and 20 min reaction time.

4.1.4.3 Effect of Reaction Time on the Growth of CVD Graphene

Based on the results presented above, a growth temperature of 850 ℃ and a gas flow rate of 6 sccm has been found to be optimum as it has shown the minimum I_D/I_G ratio and the maximum I_{2D}/I_G ratio. Since reaction time also plays a significant role in governing the quality of grown graphene, the effect of reaction time has also been investigated by considering two different reaction times of 10 and 20 min at a fixed growth temperature of 850 ℃ and acetylene flow rate of 6 sccm. The optical micrographs of synthesised graphene for 10 min and 20 min are shown in Figs. 4.10 and 4.4 (c). Figure 4.11 represents the Raman spectra of graphene grown on nickel-plated bearing steel for reaction times of 10 and 20 min. One may observe strong G and 2D peak signals along with a weak D peak for both reaction times. A slight increase in the intensity of D peak could be seen in Fig. 4.11 for a short reaction time. A decrease in growth time from 20 min to 10 min results in shifting the position of 2D peak from 2709 cm^{-1} to 2701 cm^{-1} with simultaneous increase in the intensity of 2D peak. The calculated values of I_{2D}/I_G ratio indicate a slight increase with a decrease in reaction time from 20 min to 10 min.

Fig. 4.10 Optical image of CVD-grown graphene for 10 min reaction time at 850 ℃ under an acetylene flow rate of 6 sccm.

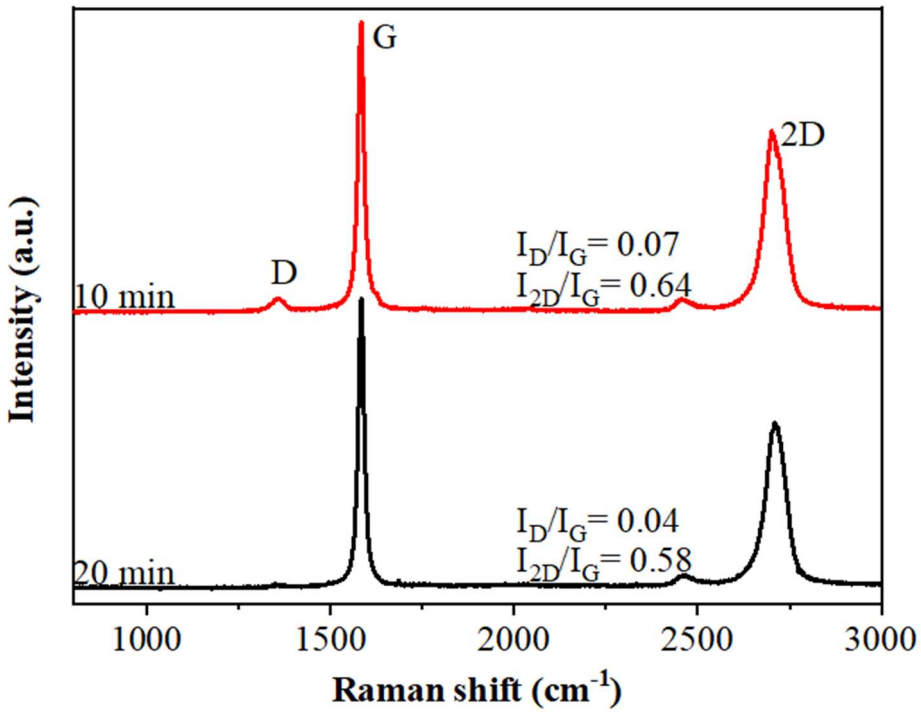

Fig. 4.11 Raman spectra of graphene grown on nickel-plated steel at 850 °C under a gas mixture 6 sccm C_2H_2 and 20 sccm of H_2 for 10 and 20 min growth time

Overall, the above mentioned results indicate that the quality of the grown graphene can be effectively controlled by regulating the reaction parameters such as growth temperature, gas flow rate, and reaction time. The optimised condition for graphene growth over nickel-plated steel has been obtained at a growth temperature of 850 °C for a reaction time of 10 min under an acetylene flow rate of 6 sccm. The optimised grown graphene has further been characterised using a 3D optical profilometer, X-ray photoelectron spectroscopy and transmission electron microscopy.

A 3D optical image of the multi-layer graphene grown on nickel-plated steel under a growth temperature of 850 °C with 6 sccm acetylene flow for a reaction time of 10 min is presented in Fig. 4.12. The root mean square roughness of the surface is found to be ~ 56 nm after the graphene coating under optimised conditions, indicating an

increase in surface roughness (roughness of the nickel-plated surface is ~ 35 nm) after the graphene deposition.

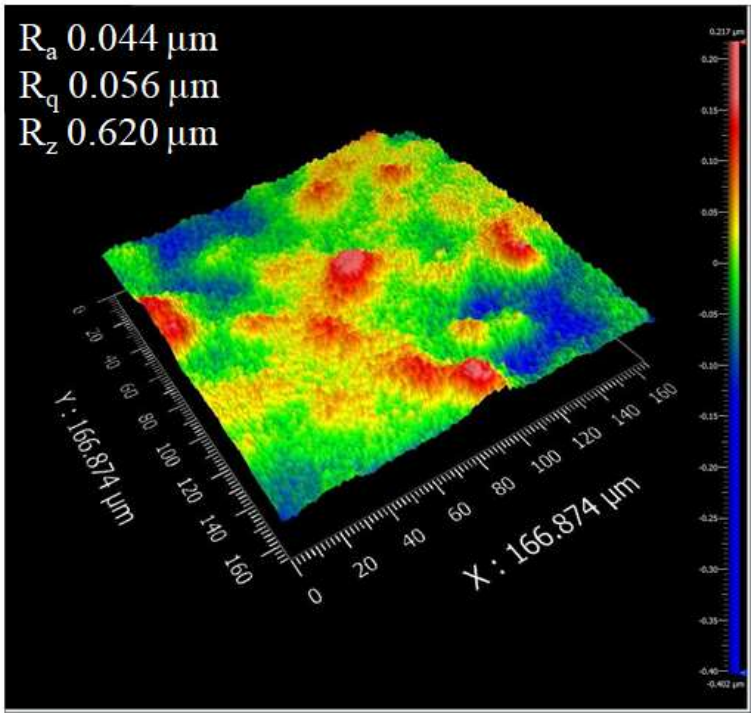

Fig. 4.12 Surface roughness of multi-layer graphene-coated steel measured by a 3D optical profilometer under a growth temperature of 850 ℃ with 6 sccm acetylene flow for a reaction time of 10 min.

Elemental composition and binding energy of the multi-layer graphene films have been determined by X-ray photoelectron spectroscopy (XPS). Figure 4.13 (a) shows a broad survey XPS spectrum of as-deposited optimised multi-layer graphene with an intense peak at 284.6 eV corresponding to C_{1s}. Two other low-intensity peaks have also been observed at 532eV and 854eV representing O_{1s} and Ni_{2p}, respectively. Further, a de-convolution of the C_{1s} spectrum of multi-layer graphene into a main peak at 284.6 eV and three other peaks centred at 285.9, 287.7, and 289 eV, respectively, has been performed and presented in Fig. 4.13 (b). Peak fitting has been done using Voigt approximation (Gaussian-Lorentzian). The binding energy of each peak and the quantitative evaluation of the fitted curve are presented in Table 4.3.

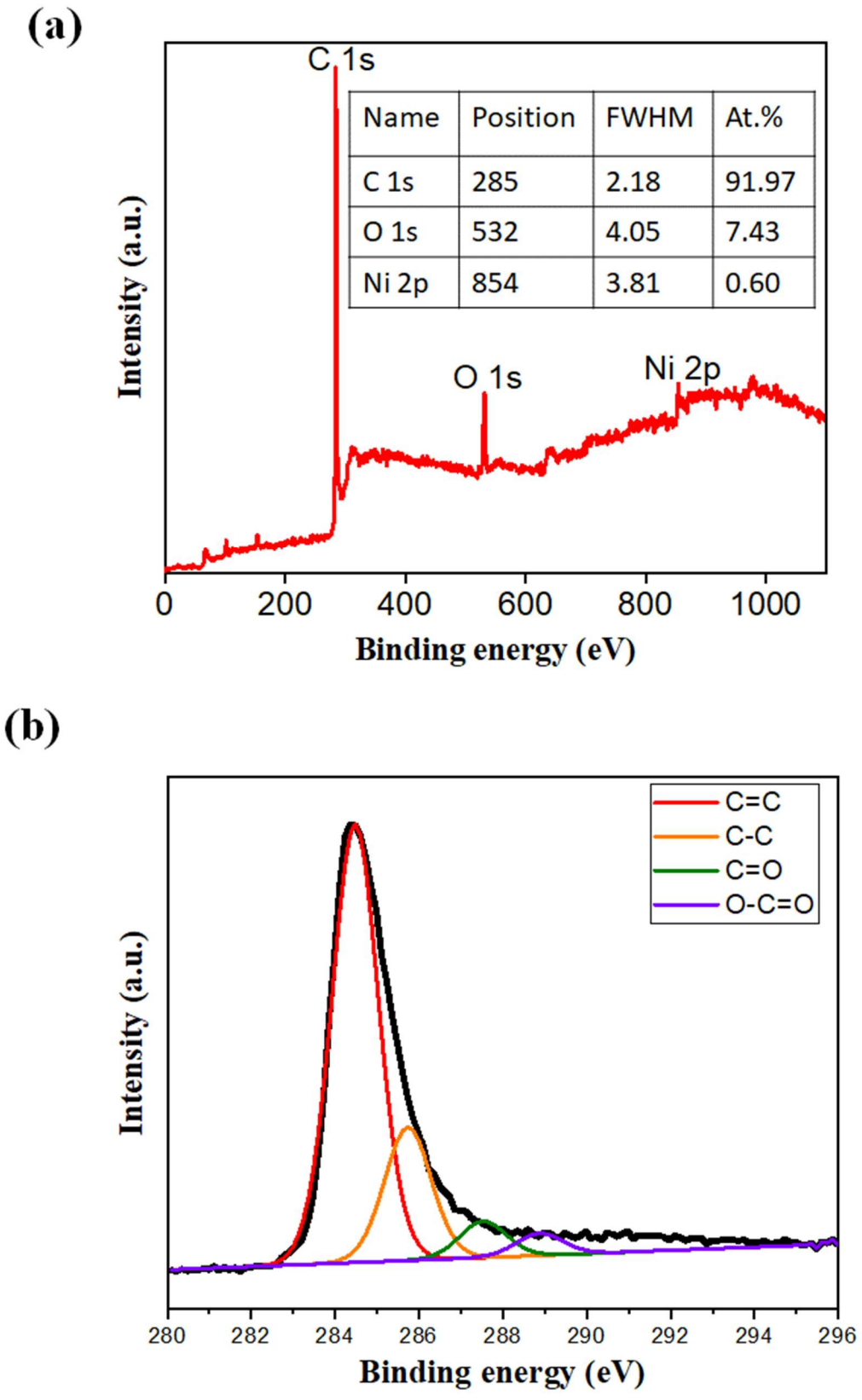

Fig. 4.13 XPS of as-deposited multilayer graphene film at 850 °C: (a) a broad XPS spectrum, and (b) C_{1s} XPS spectrum showing different peak fittings.

Table 4.3 Binding energy and quantitative analysis of peak fittings presented in Fig. 4.13.

Bonding	Position (eV)	Area	% Area
C=C	284.6	8788.23	73.10
C-C	285.9	2486.40	20.68
C=O	287.7	505.89	4.21
O-C=O	289	241.20	2.01

The transmission electron microscopy has also been employed to characterise the synthesised multi-layer graphene under a growth temperature of 850 ℃ with 6 sccm acetylene flow for a reaction time of 10 min and TEM images are given in Fig. 4.14. Focused ion beam (FIB) in-situ lift-out technique has been used to prepare the cross-sectional samples for TEM observations. Metallic layers of Cr and Pt have been deposited on the surface to prevent the damage of multi-layer graphene before the FIB process. The cross-sectional TEM of the synthesised multi-layer graphene coating shown in Fig.4.14 (a) indicates that the thickness of multi-layer graphene coating is about 21 ± 2 nm. Figure.4.14 (b) reveals a layered structure of graphene and shows the stacking of the graphene layers over each other.

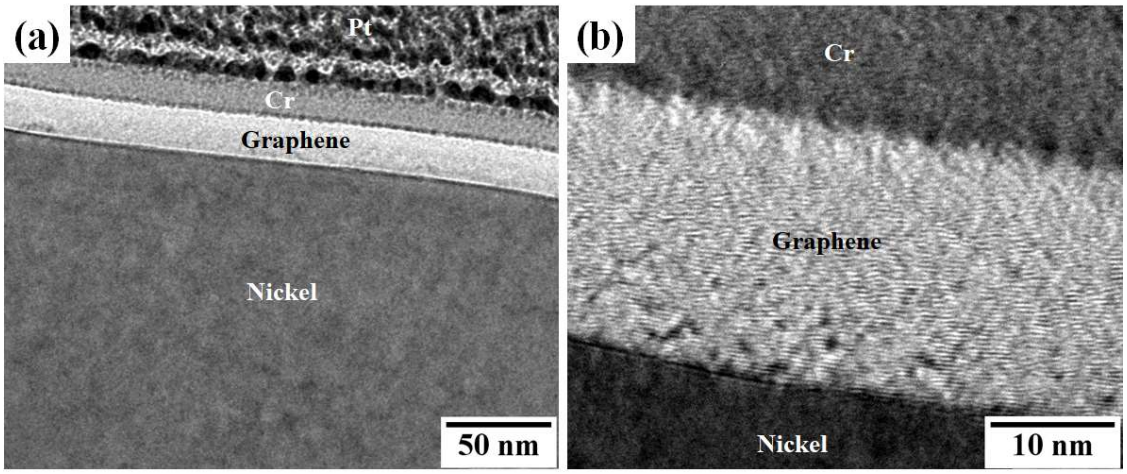

Fig. 4.14 Cross-sectional TEM images of synthesised graphene films under low (a) and high (b) magnifications revealing the thickness and layered structure of synthesised multi-layer graphene coatings.

4.1.5 TRIBOLOGICAL BEHAVIOUR OF MULTI-LAYER GRAPHENE COATINGS UNDER UNIDIRECTIONAL SLIDING

4.1.5.1 Friction Behaviour

The friction and wear behaviour of multi-layer graphene-coated bearing steel have been investigated under unidirectional sliding at a normal load of 0.5 N (corresponding to an average Hertzian contact pressure of 0.34 GPa) and a sliding speed of 0.07 m/s. The discs of base steel (chosen as reference material), nickel-plated steel, and multi-layer graphene-coated steel have been set to rotate against stationary steel ball for an initial test of 800 cycles. Figure 4.15 illustrates the variation of the coefficient of friction with number of sliding cycles. The coefficient of friction of steel ball against base steel disc is observed to be unstable and fluctuating initially for about 450 cycles and beyond that appears to have stabilised. A similar behaviour could also be seen for steel ball-nickel plated steel disc pair. However, the variation of coefficient of friction for steel ball-graphene coated steel disc pair has shown a stable trend, as evident from Fig. 4.15.

The coefficient of friction is found to be highest for the steel against base steel with a value of ~ 0.89. Electroplating of nickel over steel disc helped in reducing the coefficient of friction slightly to a value of ~ 0.66. However, a significant reduction in coefficient of friction has been observed to occur for multi-layer graphene-coated steel with an average coefficient of friction of ~ 0.15, which is approximately six times lower than that observed for base steel-steel ball tribo-pair.

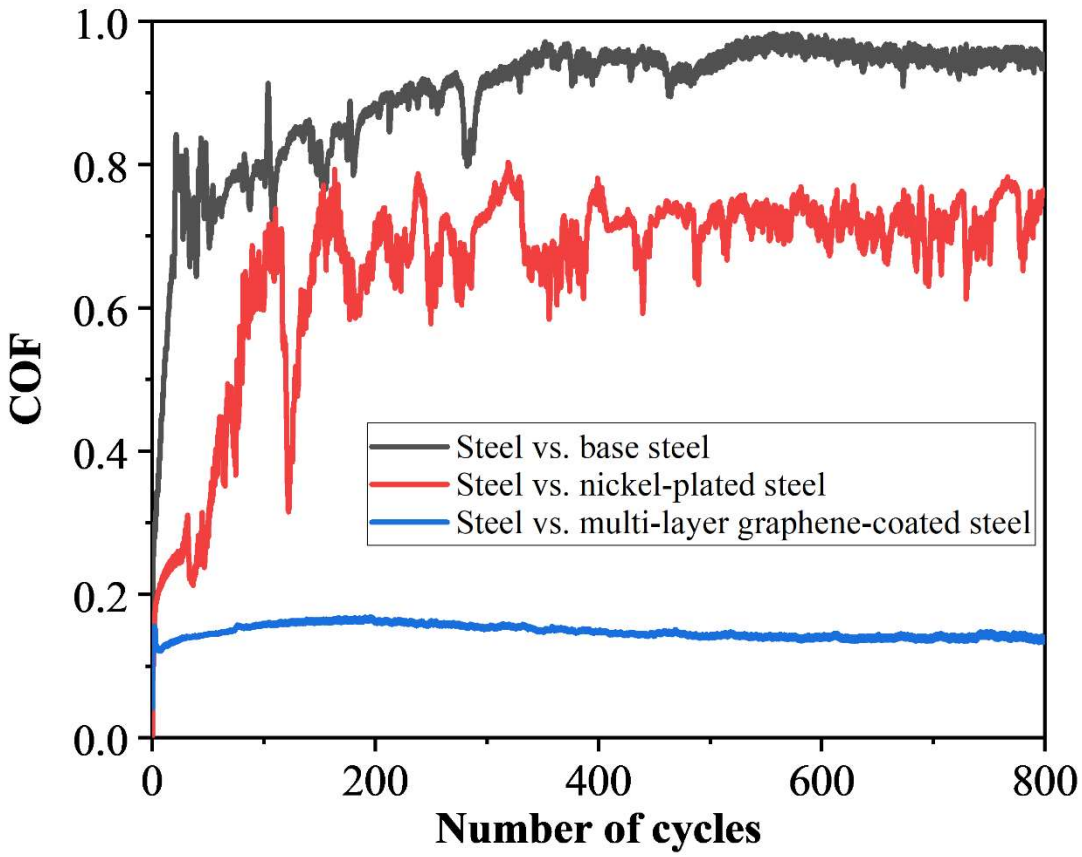

Fig. 4.15 The coefficient of friction as a function of sliding cycles of steel ball against base steel, nickel-plated steel, and multi-layer graphene-coated steel for 800 cycles at a normal load of 0.5 N.

4.1.5.2 Wear Behaviour

The worn surfaces of the discs, as well as counterpart balls, have been examined using optical microscopy, scanning electron microscopy (SEM), and EDS (energy-dispersive X-ray spectroscopy) to understand the wear behaviour of different tribo-pairs. Figures 4.16, 4.17, and 4.18 depict the optical micrographs of the worn surfaces of ball as well as disc for different tribo-pairs after the friction test. One may observe that the wear scar diameter on the ball is more significant than the respective wear track on the disc. Further, the observation of worn surfaces indicates the occurrence of severe damage to both base steel and nickel-plated steel, which could be seen in Figs. 4.16 and 4.17. Wear scar diameter and wear track width for steel ball slid against base steel (Figs 4.16 (a and b)) are found to be ~ 545 μm and ~ 429 μm, respectively. Electroplating of nickel over the surface of bearing steel has been observed to reduce the wear scar diameter and wear track width slightly for the given experimental conditions, as evident from Figs 4.17 (a and b), and the values have been found to be ~ 376 μm and ~ 330 μm, respectively. One may also observe a significant reduction in wear scar diameter and wear track width for the multi-layer graphene-coated steel – ball tribo-system with respective values of ~ 126 μm and ~ 89 μm, for wear scar and wear track as shown in Figs 4.18 (a and b). A comparison of Figs. 4.16, 4.17, and 4.18 depicts that the minimum wear scar diameter and minimum wear track width has occurred for steel-graphene coated steel tribo-pair.

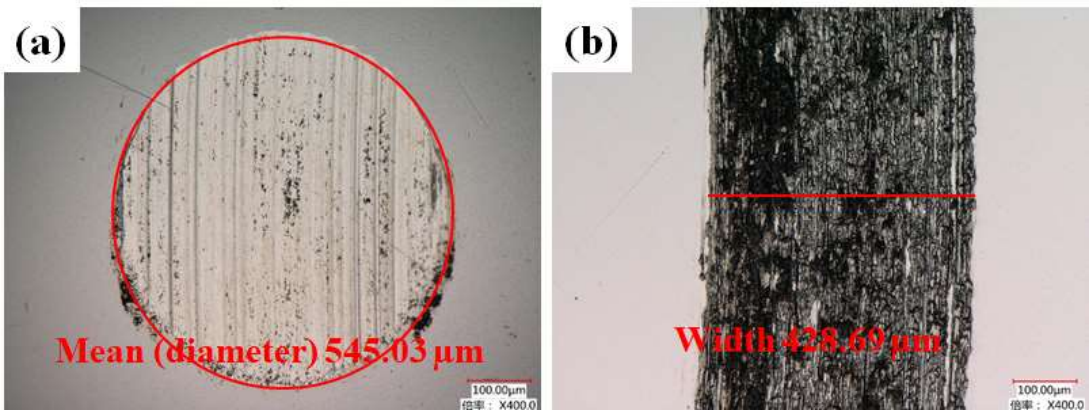

Fig. 4.16 Optical micrographs of wear scar (a) and wear track (b) on the ball and disc, respectively, for steel against base steel after the friction test of 800 cycles at a normal load of 0.5 N.

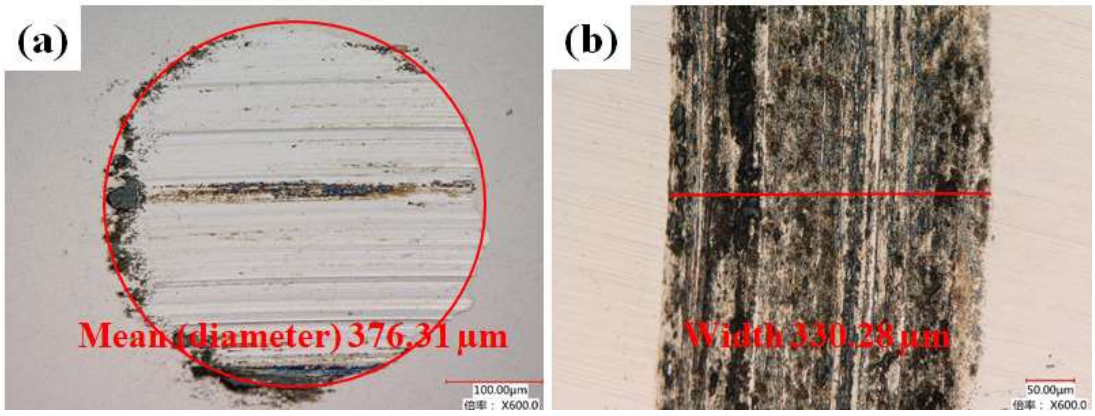

Fig. 4.17 Optical micrographs of wear scar (a) and wear track (b) on the ball and disc, respectively, for steel against nickel-plated steel after the friction test of 800 cycles at a normal load of 0.5 N.

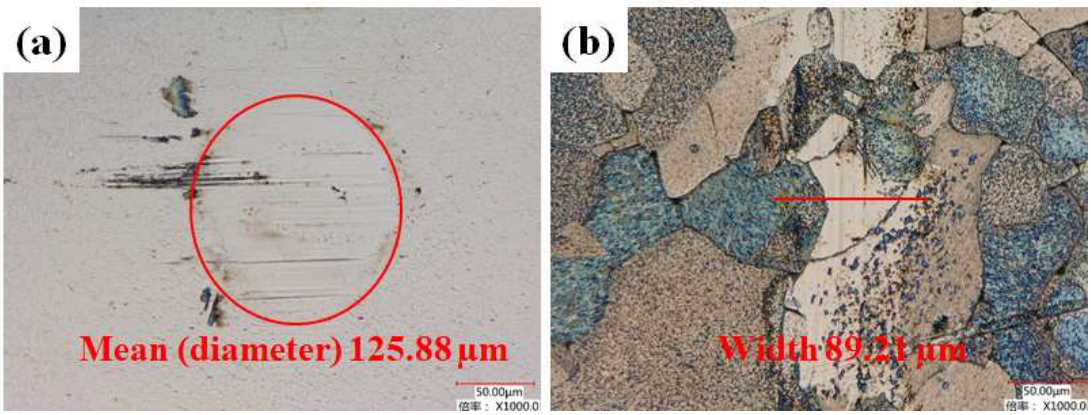

Fig. 4.18 Optical micrographs of wear scar (a) and wear track (b) on the ball and disc, respectively, for steel against multi-layer graphene-coated steel after the friction test of 800 cycles at a normal load of 0.5 N.

Figure 4.19 presents the ball wear volume and wear rate after the friction tests of 800 cycles at a normal load of 0.5 N and a sliding speed of 0.07 m/s, and the respective values are given in Table 4.4. The maximum wear rate and wear volume have been observed for steel ball used against base steel, whereas the least values for the same are observed for ball slid against graphene-coated steel. The tabulated values show that electroplating of nickel over steel reduces the ball wear by 4.4 times for short duration (800 cycles) friction tests. However, multi-layer graphene coating over nickel-plated steel has been able to reduce the wear volume by three orders of magnitude than base steel for the given test conditions. From the above results, it may be concluded that the steel ball slid against base steel disc has suffered the maximum wear, while it has undergone the least wear against multi-layer graphene-coated steel.

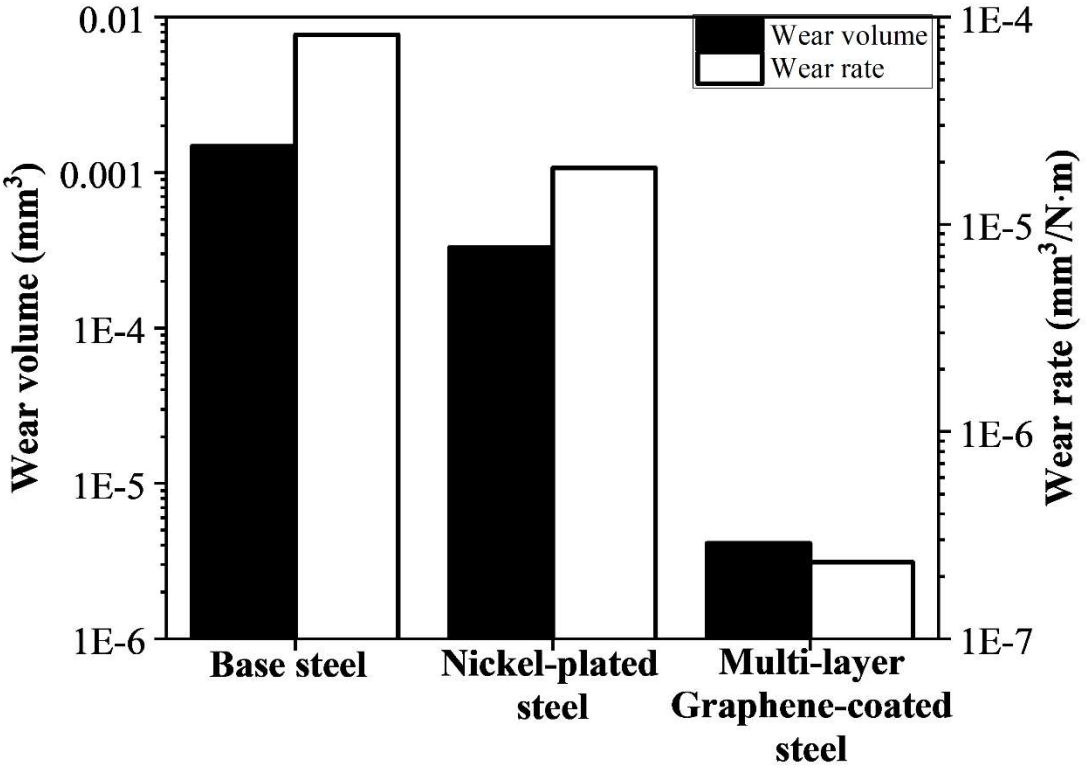

Fig. 4.19 Wear volumes and wear rates of steel ball against base steel, nickel-plated steel, multi-layer graphene-coated steel for 800 cycles.

Table 4.4 Ball wear volume calculations after the friction tests of 800 cycles at a normal load of 0.5 N load.

Tribo-pair	Wear volume (V) (800 cycles) (mm^3)	Wear rate (V/(d·L)) (800 cycles) ($mm^3/N·m$)
Steel ball vs base steel	1.45×10^{-3}	8.23×10^{-5}
Steel ball vs nickel-plated steel	3.29×10^{-4}	1.87×10^{-5}
Steel ball vs multi-layer graphene-coated steel	4.11×10^{-6}	2.34×10^{-7}

Figures 4.20, 4.21, and 4.22 show SEM images and corresponding energy-dispersive spectra of the whole worn tracks on the base steel, nickel-plated steel, and graphene-coated steel, respectively. Figure 4.20 (a) presents a deeply torn surface with scoring marks along the direction of sliding, indicating a larger wear loss due to direct metal-to-metal contact for base steel slid against steel ball. The wear appears to have taken place mainly by adhesion and abrasion, ploughing, and wear induced oxidation. The worn surface of Ni coated steel given in Fig. 4.21 (a) presents a relatively less worn out surface without significant deformation, and comparatively smaller adhesion of wear debris and reaction products (oxides) could be seen over the surface. The worn surface of multi-layer graphene-coated steel given in Fig. 4.22 (a) reveals the presence of very fine scoring marks running parallel to the sliding direction and appears to have suffered the minimum wear loss with almost negligible adhesion. The wear track is relatively smooth and abrasion appears to be a dominating mechanism as evidenced from the presence of fine grooves along the sliding direction. The EDS analysis of the wear tracks given in Figs 4.20 (b) and 4.21 (b) indicate the strong oxidation of steel and nickel-plated steel

surfaces, while the same for multi-layer graphene-coated steel reflects only mild oxidation as evident from Fig. 4.22 (b). The elemental analysis also suggests a significant increase in carbon content in wear track of multi-layer graphene-coated steel compared to other wear tracks.

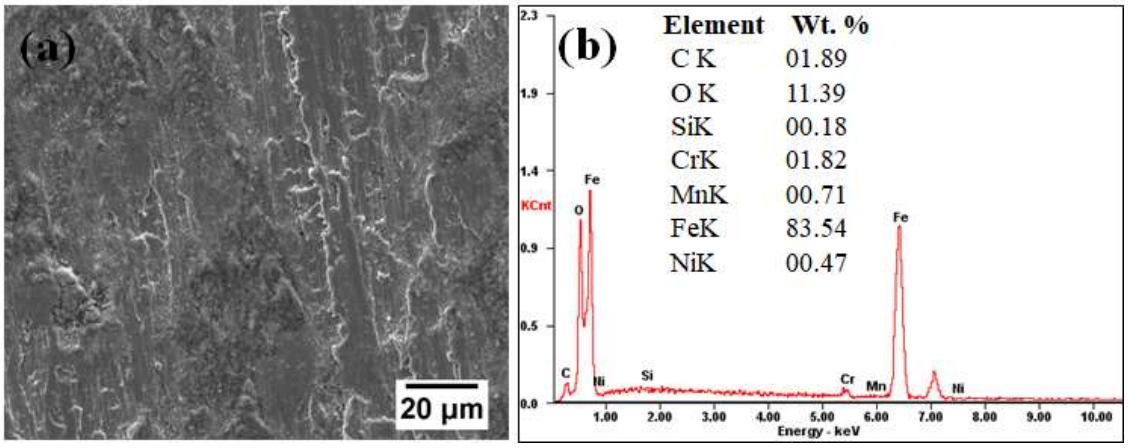

Fig. 4.20 SEM image and corresponding energy dispersive spectroscopy (EDS) analysis of wear track on the base steel disc after the friction test of 800 cycles at a normal load of 0.5 N.

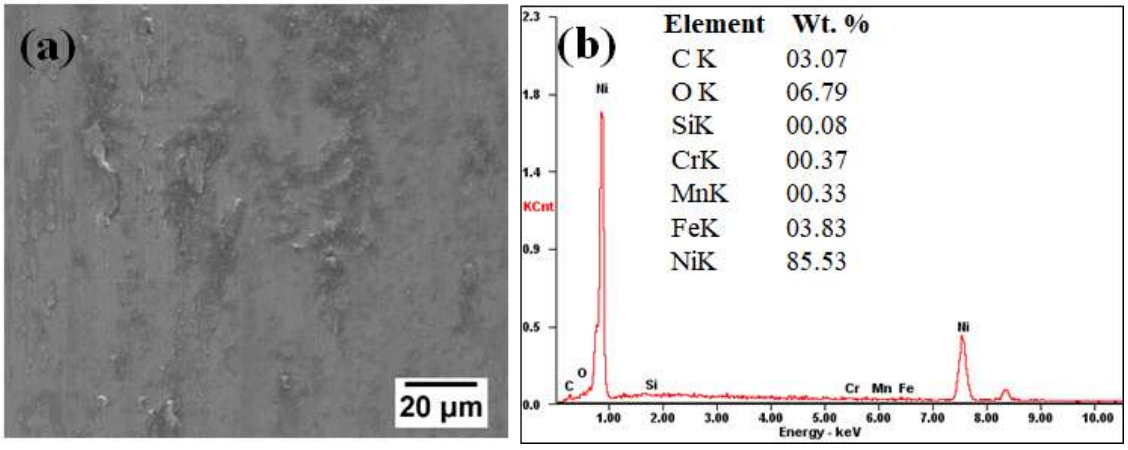

Fig. 4.21 SEM image and corresponding energy dispersive spectroscopy (EDS) analysis of wear track on the nickel-plated steel disc after the friction test of 800 cycles at a normal load of 0.5 N.

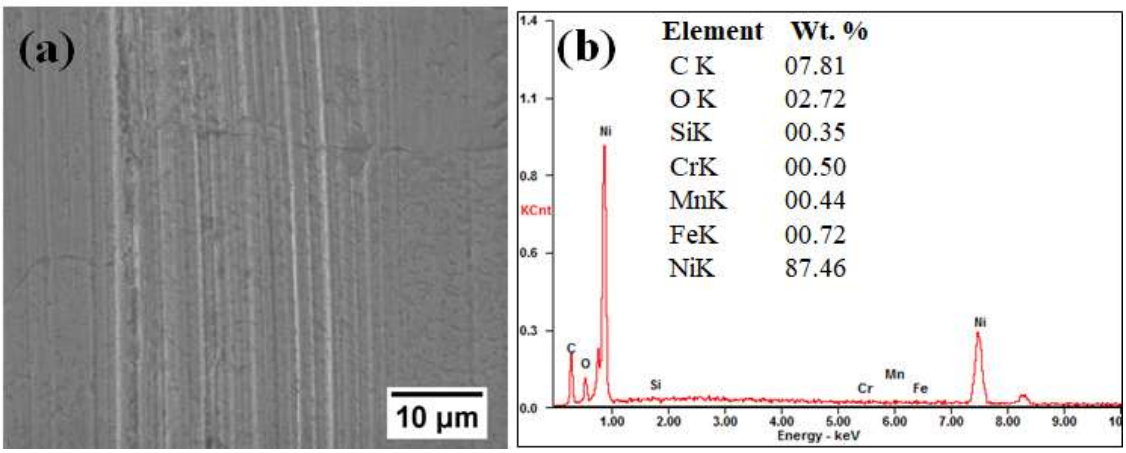

Fig. 4.22 SEM image and corresponding energy dispersive spectroscopy (EDS) analysis of wear track on the multi-layer graphene-coated steel disc after the friction test of 800 cycles at a normal load of 0.5 N.

The SEM micrographs of counterpart steel balls after the sliding tests under the normal load of 0.5 N are presented in Fig. 4.23 and Table 4.5 shows the chemical composition of different areas of wear scar (mentioned in Fig. 4.23) obtained through the EDS. One may observe a significant reduction in wear scar for multi-layer graphene-coated steel in comparison to both base and nickel-plated steel.

Raman spectroscopy analysis has been performed to confirm the existence of graphene on steel surface even after dry sliding friction tests and also to confirm the transfer of the graphene layer on the counter surface, i.e., ball. Figure 4.24 presents the typical Raman spectra of worn surfaces after the friction tests of 800 cycles and their respective locations on the optical images of worn surfaces. Raman spectra from different locations on wear track are presented in Fig. 4.24 (b) with respective locations marked in Fig. 4.24 (a). Points 1 and 10 are outside the wear tracks, while other points are inside the wear track. The presence of D, G, and 2D peaks can be clearly observed in the Raman spectrum for every point. However, an increase in D peak can also be observed for each point on the disc surface compared to that obtained for as-deposited optimised multi-layer

graphene on disc surface (Fig. 4.11). Further, the wear scar of the steel ball slid against multi-layer graphene-coated steel has also been analysed by Raman spectroscopy at the marked locations (1 and 2) in Fig. 4.24 (c) and corresponding spectra are illustrated in Fig. 4.24 (d). One may observe the presence of all three characteristics peaks, i.e., (D, G, and 2D) for both the locations. Similar to Raman spectra on wear track, an increase in D peaks occurs at both marked points on the wear scar, which reflects the incorporation of defects in graphene during the sliding tests.

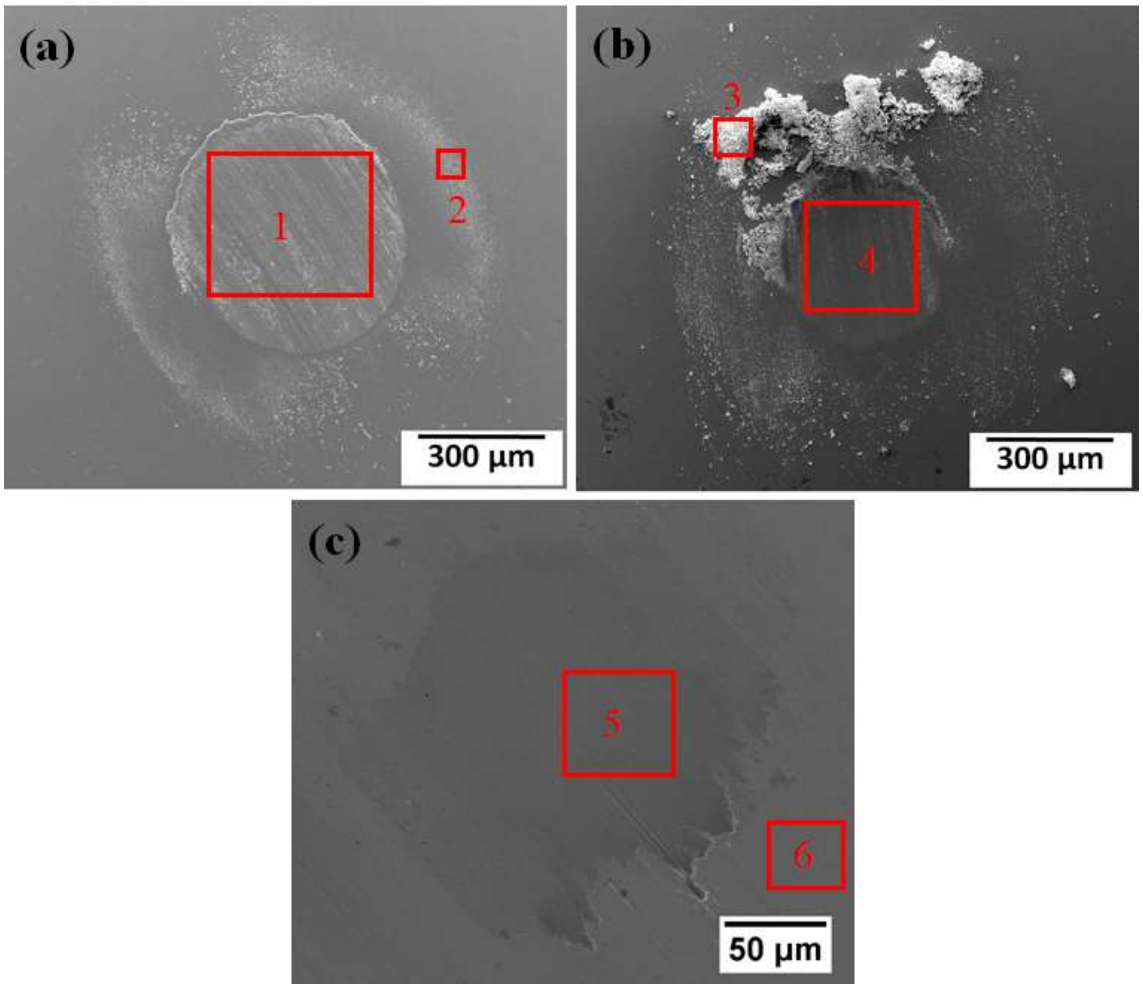

Fig. 4.23 SEM images of the worn counterpart surfaces (balls) slid against (a) base steel, (b) nickel-plated steel, and (c) multi-layer graphene-coated steel after the friction tests of 800 cycles under the normal load of 0.5 N.

Table 4.5 EDS analysis of wear surface after the friction test of 800 cycles.

EDS area	Chemical composition (wt.%)						
	C	**O**	**Fe**	**Cr**	**Ni**	**Mn**	**Si**
Point 1	1.62	3.00	91.02	2.06	1.21	0.73	0.37
Point 2	1.54	21.50	73.90	1.43	0.72	0.60	0.31
Point 3	1.46	2.57	90.59	1.89	2.24	0.81	0.44
Point 4	1.72	17.66	39.36	1.15	39.58	0.28	0.25
Point 5	2.01	1.81	92.48	2.06	0.70	0.58	0.30
Point 6 (Ball Blank)	0.90	1.18	93.73	1.99	0.87	0.86	0.47

4.1.5.3 Friction and Wear Behaviour of Grown Graphene for Long Duration Sliding

To investigate the longevity of multi-layer graphene coating on the steel over time, the tribo-tests have also been conducted for a longer duration of 5600 cycles under a normal load of 0.5 N and a sliding speed of 0.07 m/s. Figure 4.25 presents the variation of coefficient of friction for steel against base steel, steel against nickel-plated steel, and steel against multi-layer graphene-coated steel tribo-pairs with number of cycles. For steel against base steel, the coefficient of friction remains high and fluctuating with an average value of ~ 0.8. It can be observed from Figure 4.25 that for the initial 1000 cycles, the coefficient of friction of steel against nickel-plated steel is lower than that of steel against base steel, but after that, it increases and attains a slightly higher value in comparison to

that observed for the steel against base steel system. However, a significant reduction in coefficient of friction could be observed for the steel against multi-layer graphene-coated steel from the beginning of the test, and an average value of ~ 0.18 has been recorded for coefficient of friction throughout the friction test, which is slightly more than that of short duration sliding (Fig. 4.15). This increase may be attributed to the loss of the beneficial effect of graphene with time.

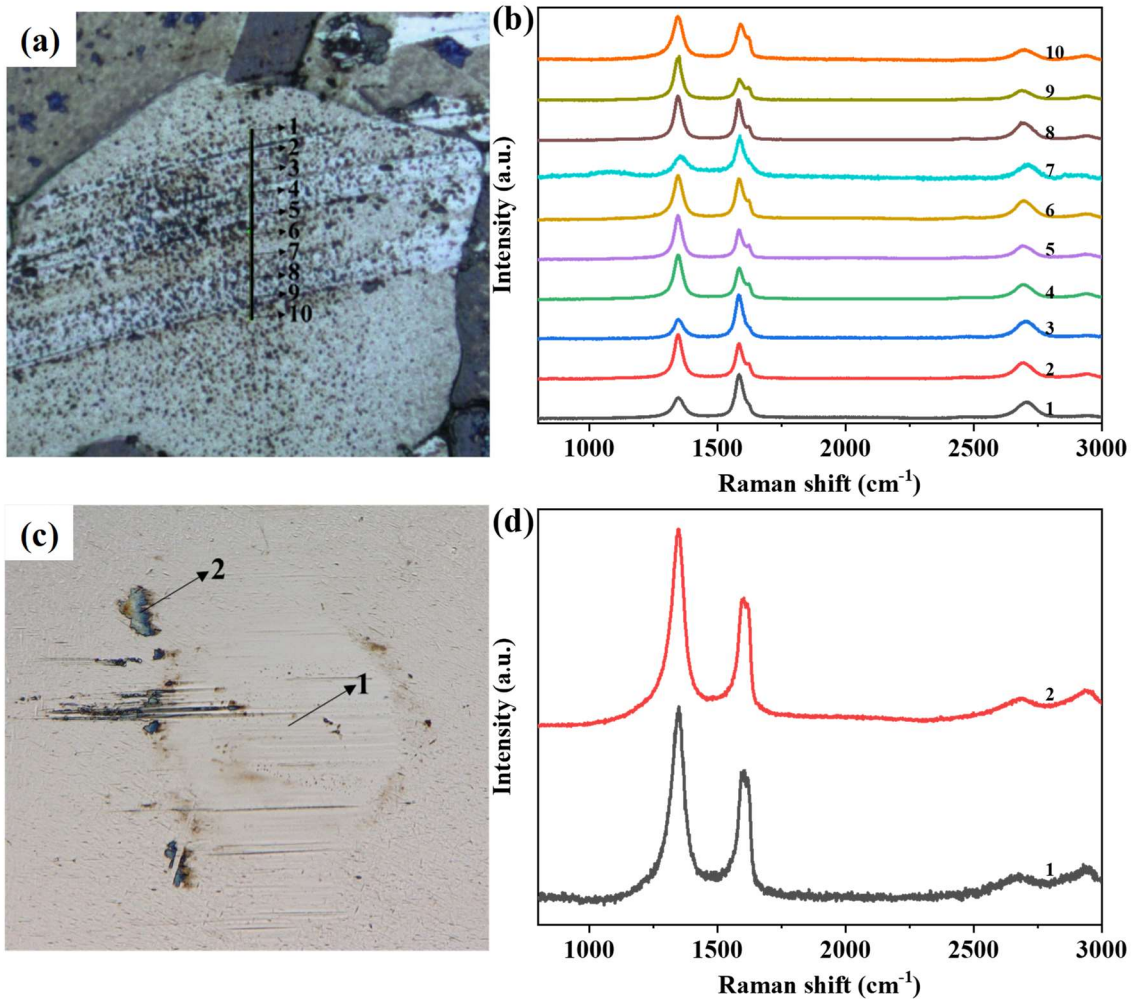

Fig. 4.24 Optical micrographs and the corresponding Raman analysis of wear track (a, b) and wear scar (c, d) for 800 cycles.

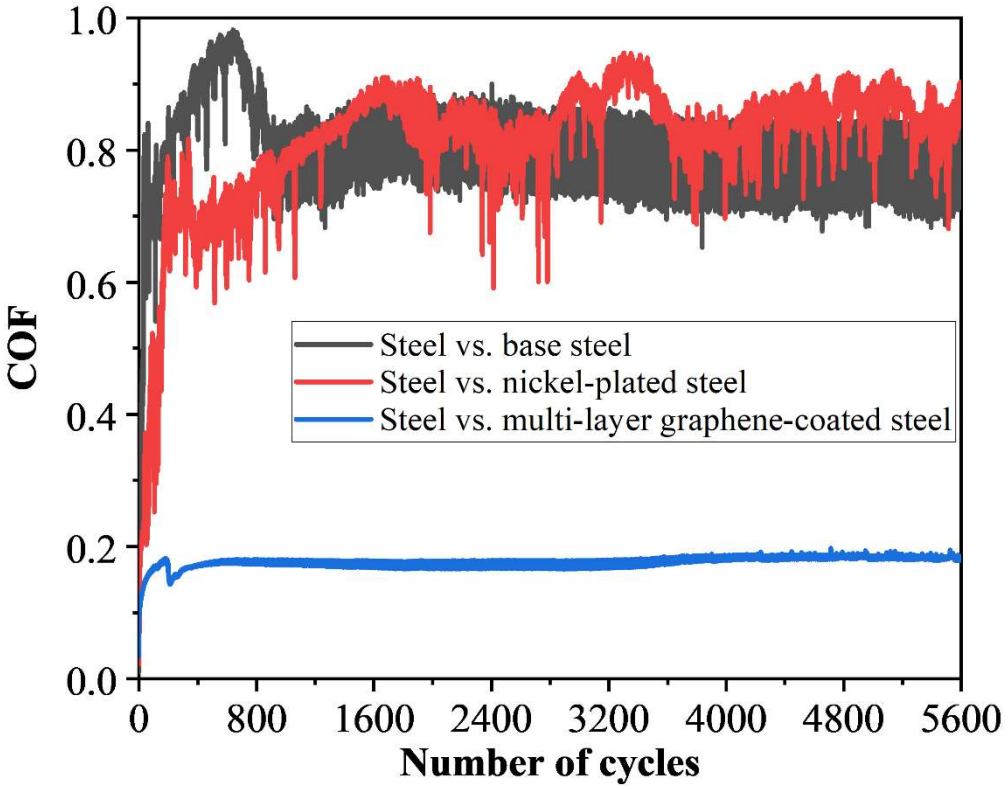

Fig. 4.25 Coefficients of friction as a function of sliding cycles and (b) wear volumes and wear rates of steel ball against steel, Nickel-plated steel, Multi-layer graphene-coated steel for 5600 cycles.

Figures 4.26, 4.27, and 4.28 present the optical micrographs of the worn surfaces after the friction tests of 5600 cycles for different combinations of tribo-pairs (ball and disc) under a load of 0.5 N with the sliding speed of 0.07 m/s. It is clear from Fig. 4.26 that the high coefficient of friction causes substantial wear of rubbing surface for steel ball against base steel. A wear scar diameter of ~ 850 µm and a wear track width of ~ 690 µm have been observed for the steel against base steel, while these values reduced to ~ 757 µm and ~ 566 µm, respectively, after the electroplating of nickel on the steel surface (Fig. 4.27). The wear scar diameter is observed to reduce to ~ 167 µm with the corresponding reduction in wear track width to ~ 149 µm for multi-layer graphene-coated steel, as shown in Fig. 4.28.

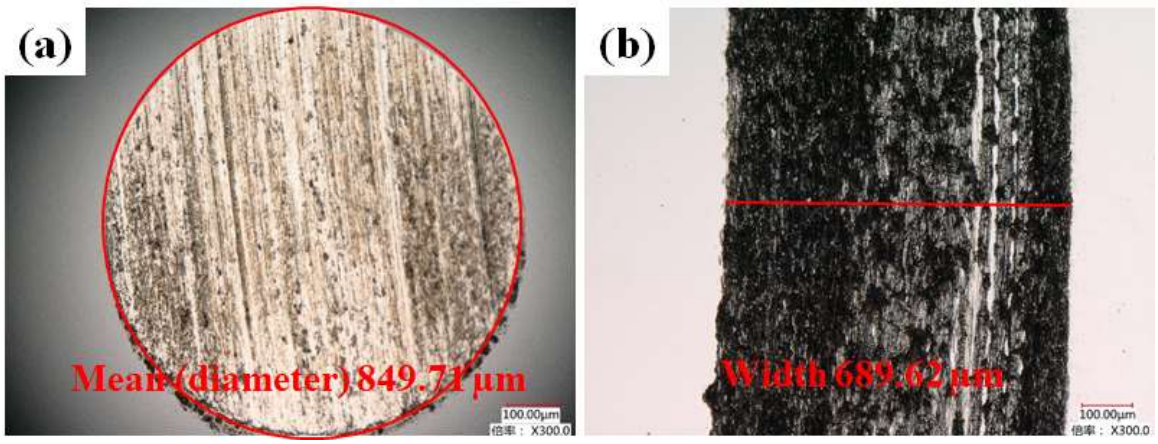

Fig. 4.26 Optical micrographs of wear morphologies of the ball (a) and disc (b) counter-pairs for steel against base steel after the friction test of 5600 cycles.

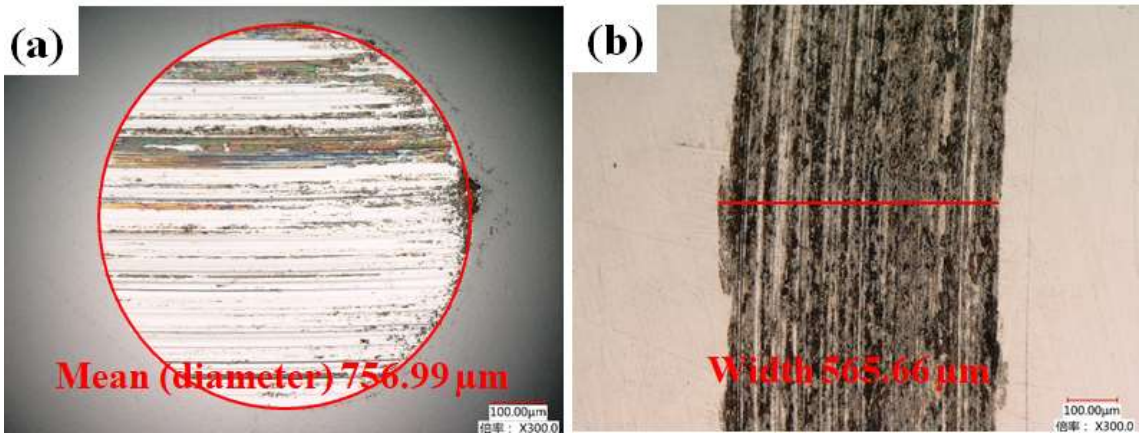

Fig. 4.27 Optical micrographs of wear morphologies of the ball (a) and disc (b) counter-pairs for steel against nickel-plated steel after the friction test of 5600 cycles.

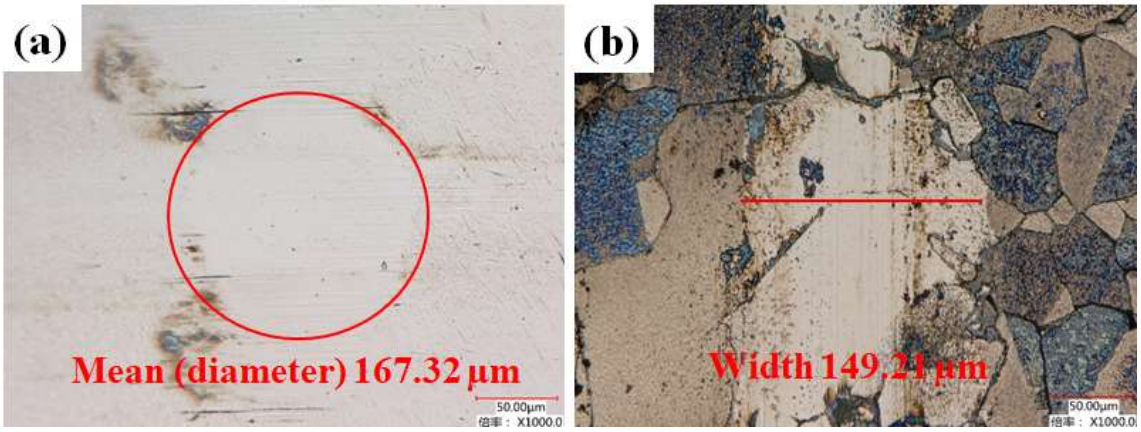

Fig. 4.28 Optical micrographs of wear morphologies of the ball (a) and disc (b) counter-pairs for steel against multi-layer graphene-coated steel after the friction test of 5600 cycles.

Figure 4.29 presents the ball wear volume and wear rate for long duration (5600 cycles) friction tests under a normal load of 0.5 N with a sliding speed of 0.07 m/s, and respective values are given in Table 4.6. The maximum wear rate and wear volume have been observed for steel ball slid against base steel. The electroplating of nickel over steel has found to reduce the ball wear volume by 1.5 times (approx.) in comparison to that observed for steel on base steel tribo-pair. However, the minimum wear volume and wear rate have been observed for the ball slid against multi-layer graphene-coated steel and these are, respectively, 2 and 3 orders of magnitude less than those observed for ball slid against base steel. The reduction in wear volume reflects the ability of graphene to provide effective lubrication even for a longer duration under atmospheric conditions.

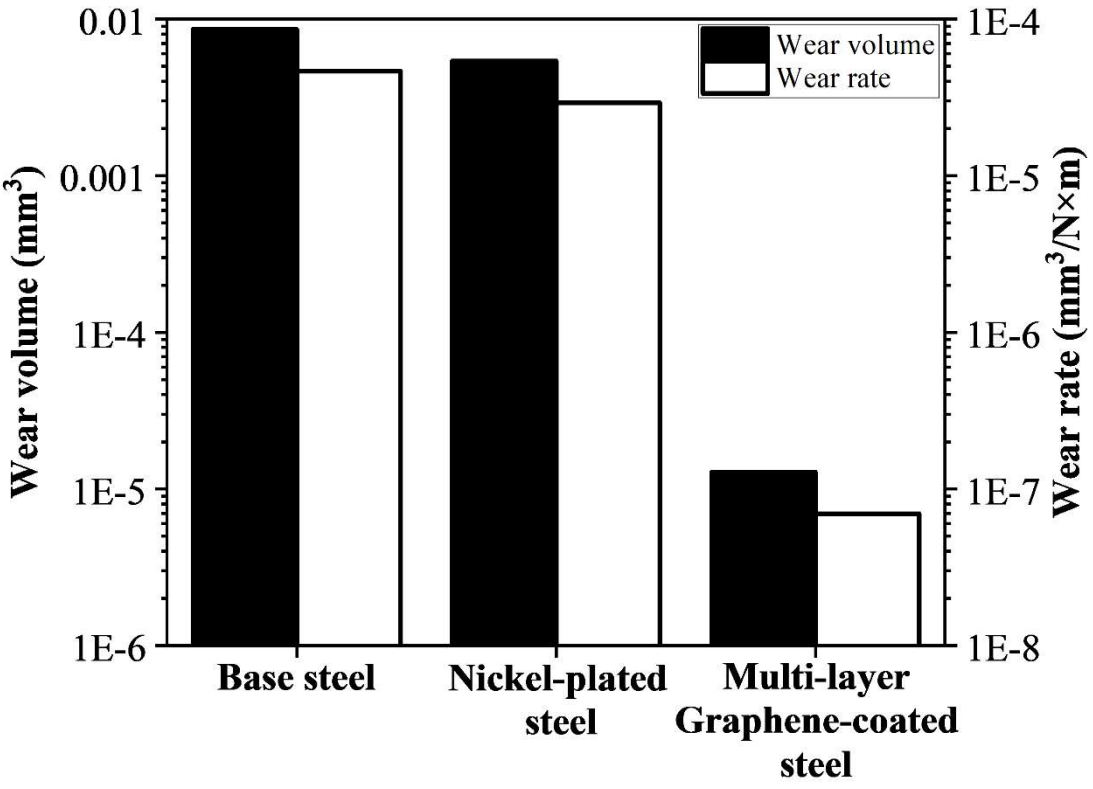

Fig. 4.29 Wear volumes and wear rates of steel ball against base steel, nickel-plated steel, multi-layer graphene-coated steel for 5600 cycles.

Table 4.6 Ball wear volume calculations after the friction tests of 5600 cycles at a normal load of 0.5 N load.

Tribo-pair	**Wear volume (V) (5600 cycles) (mm^3)**	**Wear rate (V/(d·L)) (5600 cycles) ($mm^3/N·m$)**
Steel ball vs base steel	8.59×10^{-3}	4.65×10^{-5}
Steel ball vs nickel-plated steel	5.40×10^{-3}	2.92×10^{-5}
Steel ball vs multi-layer graphene- coated steel	1.28×10^{-5}	6.94×10^{-8}

Figure 4.30 shows the SEM images of wear tracks on the discs and respective wear scar on the ball. Figure 4.30 (a) shows the significant damage for base steel slid against steel ball indicative of the occurrence of adhesion due to direct metal-to-metal contact along with a compacted layer of wear debris and some regions from where the layer appears to have detached. Figure 4.30 (b) also reveals a severely damaged worn surface of the ball and the presence of wear debris on the periphery of the wear scar. The worn surface of the nickel-plated steel disc presented in Fig. 4.30 (c) appears to be covered by a transfer layer of wear debris along with the presence of adhered lumps of wear debris at few locations whereas the worn surface of the ball slid against Ni-coated steel depicted in Fig. 4.30 (d) shows scoring marks running parallel to the direction of sliding along with accumulated debris, which seems to be adhered at the periphery. The worn surface of graphene-coated steel illustrated in Fig. 4.30 (e) presents some wide and shallow scoring marks indicative of mild abrasion. Figure 4.30 (f) showing the SEM image of steel ball slid against multi-layer graphene-coated steel also presents a very smooth surface with no obvious scoring marks.

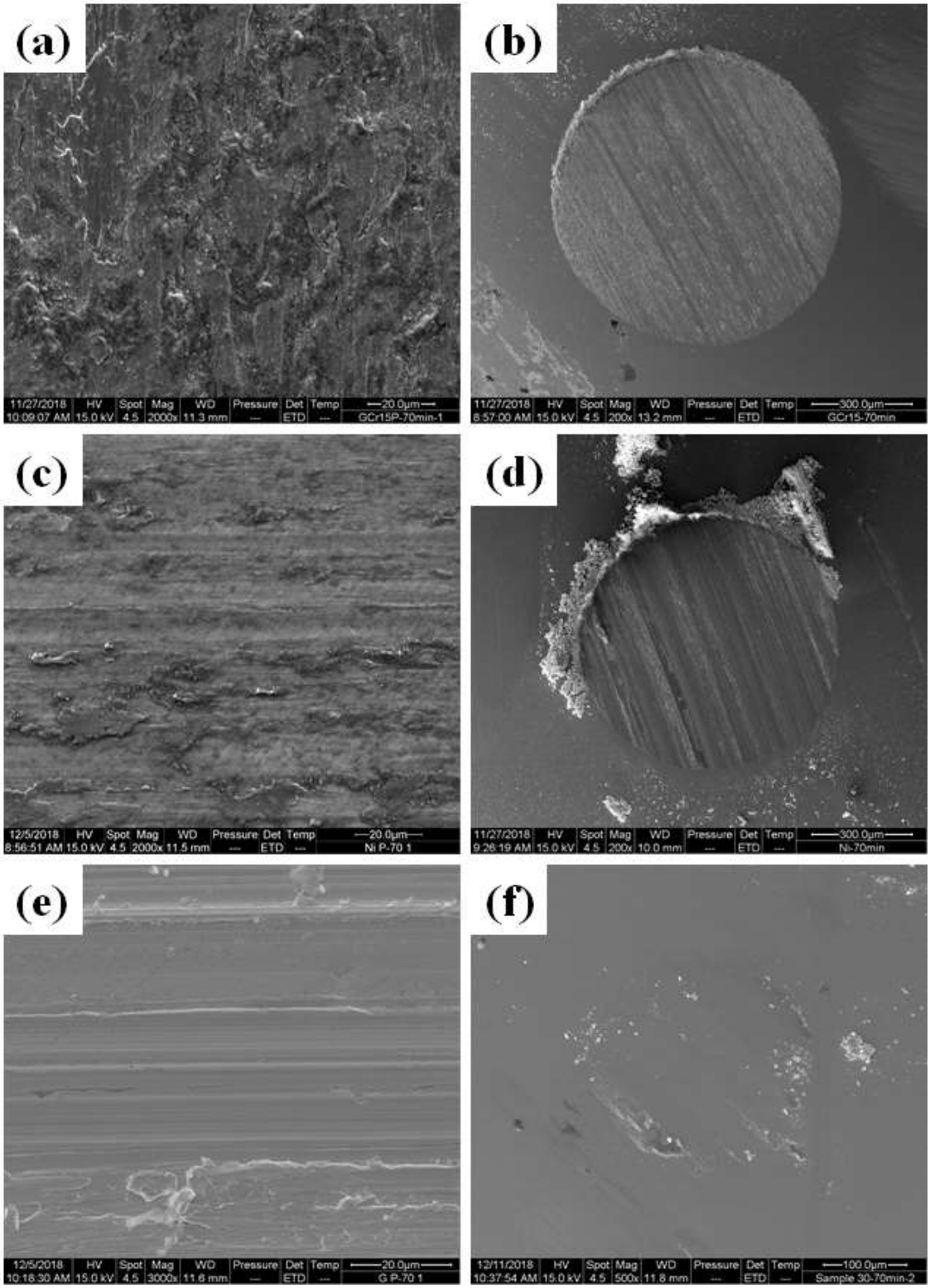

Fig. 4.30 SEM images of wear tracks (a, c, and e) on the disc and respective wear scar (b, d, and f) on the ball for steel-base steel (a and b), steel-nickel plated steel (c and d), and steel-graphene coated steel (e and f) tribo-pair after the friction test of 5600 cycles at a normal load of 0.5 N.

Figure 4.31 presents the typical Raman spectra of the worn surface of the multi-layer graphene-coated steel disc, and corresponding wear scar on the ball after the friction tests of 5600 cycles under the normal load of 0.5 N. The presence of D, G, and 2D peaks in the Raman spectrum of disc surface indicates the presence of graphene over the steel surface even after sliding for 5600 cycles. The Raman spectrum of the worn surface of the ball also reveals the presence of D, G, and 2D peak, which suggests the transfer of graphene on the ball surface during the sliding. Although an intense D peak for both ball and disc has been observed, which indicates a significant increase of defects in graphene during the sliding tests.

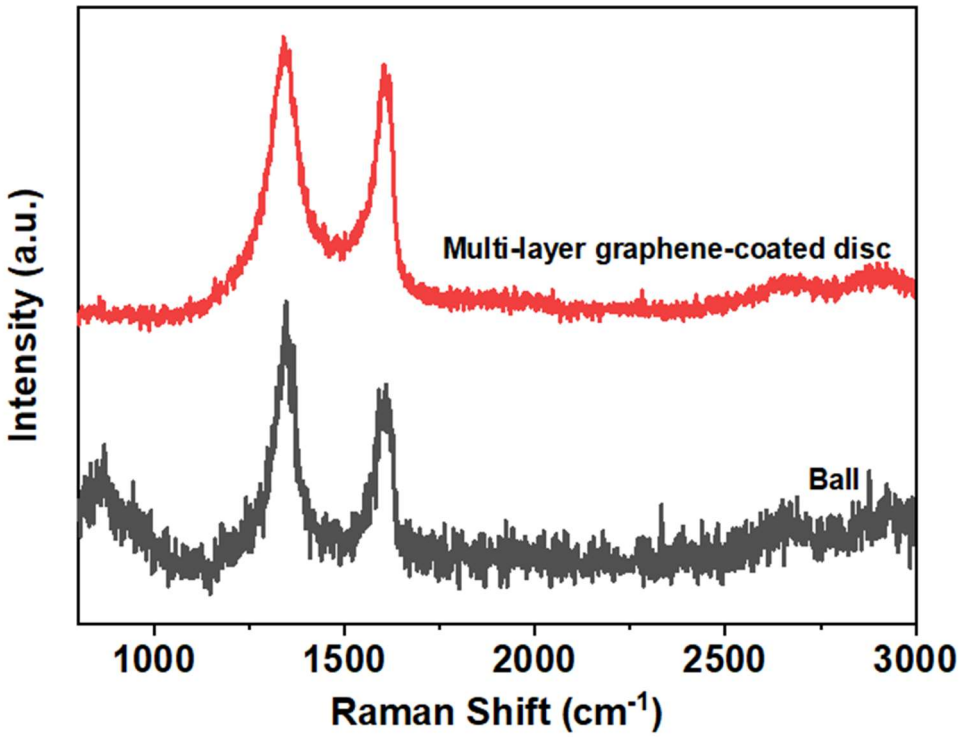

Fig. 4.31 Raman spectra of the wear track (disc) and wear scar (ball) for 5600 cycles.

4.1.6 TRIBOLOGICAL BEHAVIOUR OF MULTILAYER GRAPHENE COATINGS UNDER RECIPROCATING SLIDING

4.1.6.1 Friction Behaviour

The friction and wear behaviour of multi-layer graphene-coated bearing steel have also been investigated under reciprocating sliding at a normal load of 0.5 N (corresponding to an average Hertzian contact pressure of 0.34 GPa) and a sliding speed of 0.01 m/s. The discs of base steel (chosen as a reference material), nickel-plated steel, and multi-layer graphene-coated have been set to reciprocate against stationary steel ball for a test of 600 cycles. Figure 4.32 illustrates the variation of coefficient of friction with the number of sliding cycles. The coefficient of friction of steel ball against base steel disc is observed to be highly unstable and fluctuating throughout the friction test, whereas the same for steel ball-nickel-plated steel disc system is observed to be fluctuating for nearly 100 cycles, but gets stabilised later with very small amplitude of fluctuations. However, the variation of the coefficient for steel ball-graphene coated steel disc pair has shown a stable trend with almost no fluctuations, as evident from Fig. 4.32. The coefficient of friction is found to be the highest for the steel ball- base steel tribo-pair with a value of ~ 0.74. The nickel-plating over the steel disc reduced the friction (~ 0.59) and fluctuations to some extent, as evident from Fig. 4.32. However, a significant reduction in coefficient of friction is found to occur for multi-layer graphene-coated steel, which has shown a coefficient of friction of ~ 0.15, i.e., approximately five times lower than that observed for base steel-steel tribo-pair.

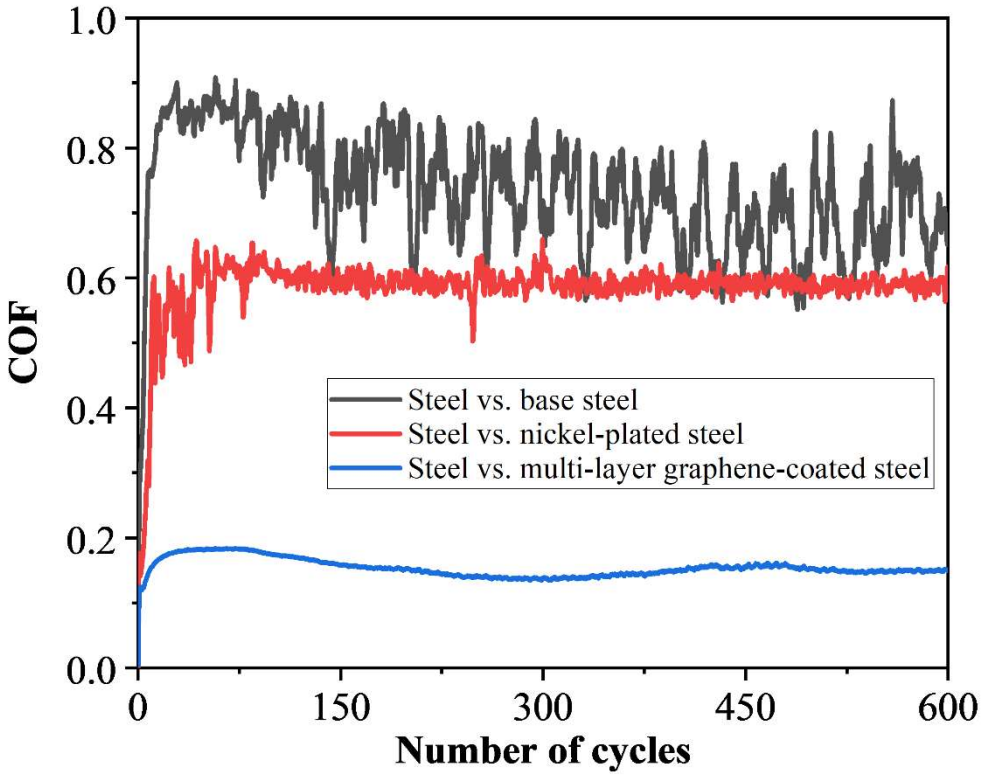

Fig. 4.32 The coefficients of friction as a function of sliding cycles of steel ball against base steel, nickel-plated steel, and multi-layer graphene-coated steel for 600 cycles at a normal load of 0.5 N.

4.1.6.2 Effect of Normal Load on Friction Behaviour

In order to examine the durability of multi-layer graphene coating under different loads, the tribo-tests have been conducted for 600 cycles under different normal loads of 0.1, 0.3, 0.5, and 1 N (corresponding to Hertzian contact pressures of 0.2, 0.28, 0.34 and 0.42 GPa, respectively) and a sliding speed of 0.01 m/s. Figure 4.33 illustrates the variation of coefficient of friction for steel ball-graphene-coated steel tribo-systems with the number of cycles at different loads. The coefficient of friction is found to decrease with the increasing normal load from 0.1 to 0.5 N. The average value of the coefficient of friction under a normal load of 0.1 N has been found to be ~ 0.19, whereas the same for 0.3 and 0.5 N are observed to be ~ 0.17 and ~ 0.15, respectively. The coating

appears to have failed after 250 cycles at a normal load of 1 N, as seen from a sharp rise in coefficient of friction presented in Fig.4.33. However, the minimum average coefficient of friction of 0.13 is observed for 1 N load till 250 cycles and it shoots up sharply to a value of 0.9 beyond that as indicated in Fig. 4.33 before attaining a value of ~ 0.6 for the remaining duration of test.

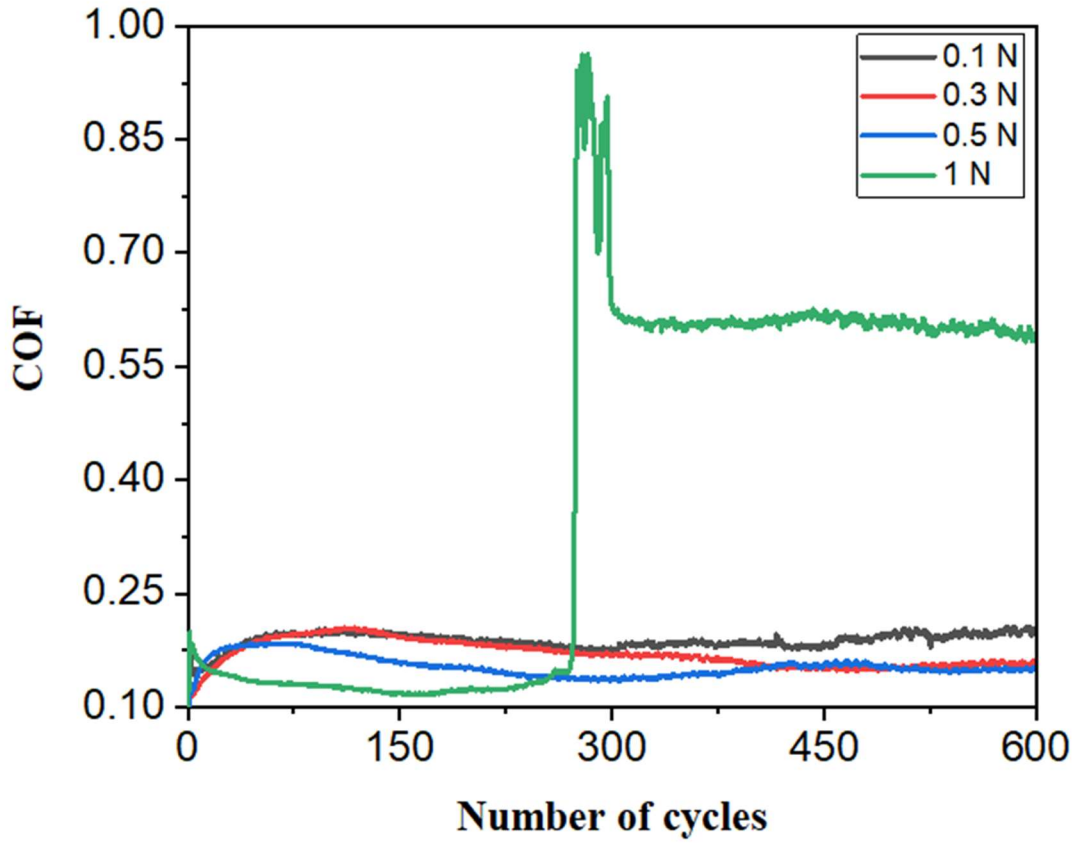

Fig. 4.33 Coefficient of friction as a function of sliding cycles under different loads for multi-layer graphene-coated steel.

Figure 4.34 depicts the variation of average coefficient of friction with normal load for steel-base steel, steel-nickel-plated steel, and steel-multi-layer graphene-coated steel tribo-pairs. The coefficient of friction increases with an increase in load for base steel as well as nickel-plated steel. However, the coefficients of friction shown by steel-

nickel-plated steel tribo-pair are lower than those observed for the steel-base steel system under all the loads used in the study. The average coefficients of friction at 0.1, 0.3, 0.5, and 1 N have been found to be 0.61, 0.69, 0.74, and 0.84, respectively, for steel-base steel system, whereas the same for steel-nickel-plated steel are found to be 0.53, 0.56, 0.59, and 0.61, respectively. In contrast, the average coefficient of friction for steel-multi-layer graphene-coated steel tribo-systems has been observed to decrease with increasing load from 0.1 to 0.5 N, followed by an increase for 1 N as evident from Fig. 4.34. One may also observe a significant reduction in the coefficient of friction for graphene-coated steel in comparison to both the base and nickel-plated steel, reflecting the lubricious effect of graphene.

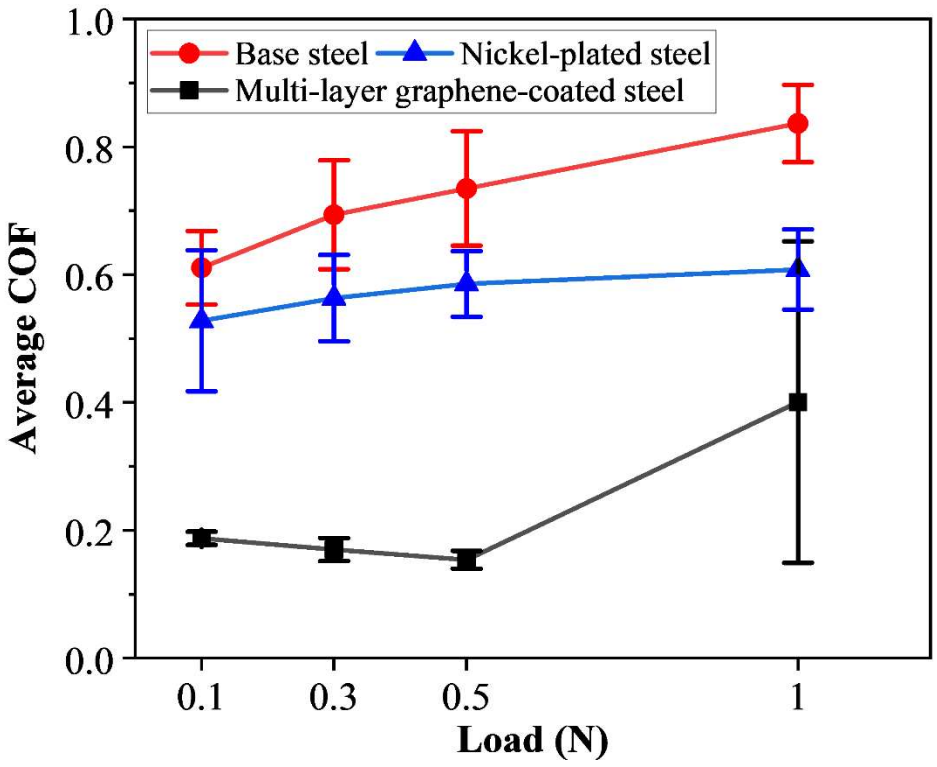

Fig. 4.34 Variation of the average coefficient of friction with applied normal load for base steel, nickel-plated steel, and multi-layer graphene-coated steel.

4.1.6.3 Wear Behaviour

The worn surfaces of the discs as well as counterpart balls have been examined under an optical microscope and scanning electron microscope to understand the wear behaviour of different tribo-pairs. Figures 4.35, 4.36, and 4.37 show the optical micrographs of the worn surfaces of ball as well as disc for different tribo-pairs after the friction tests of 600 cycles under a load of 0.5 N. One may observe that the worn surfaces of both base steel and nickel-plated steel have undergone relatively severe damage compared to that of multi-layer graphene-coated steel, which could be judged from a comparison of Figs. 4.35, 4.36, and 4.37. Wear scar diameter and wear track width for steel ball against base steel disc (Figs. 4.35 (a and b)) are found to be ~ 262 μm and ~ 244 μm, respectively, whereas the same are found to be ~ 199 μm and ~ 170 μm, respectively for steel ball against nickel-plated steel disc as evident from Figs 4.36 (a and b). Further, a significant reduction in both wear scar diameter and wear track width is found to occur for steel- graphene-coated steel tribo-system with respective values of ~ 99 and ~ 92 μm, as shown in Figs. 4.37 (a and b), respectively. Figure 4.38 shows the optical micrographs of worn surfaces of ball and multi-layer graphene-coated steel after the friction tests of 600 cycles under a load of 1 N. The graphene coating appears to have been damaged significantly, exposing thereby the underlying substrate, which might have resulted in an increase in wear scar diameter and wear track width to ~ 233 μm and ~ 210 μm, as evident from Figs. 4.38 (a and b).

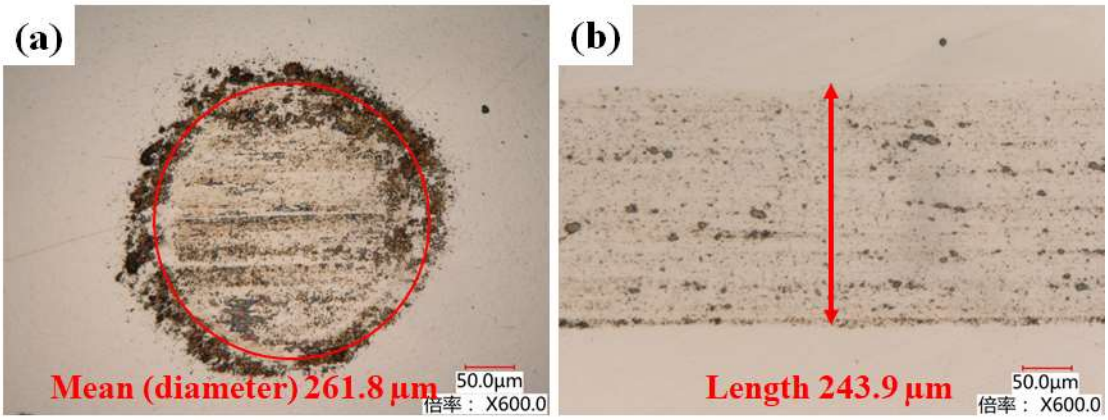

Fig. 4.35 Optical micrographs of wear scar (a) and wear track (b) on the ball and disc, respectively, for steel against base steel after the friction test of 600 cycles at a normal load of 0.5 N.

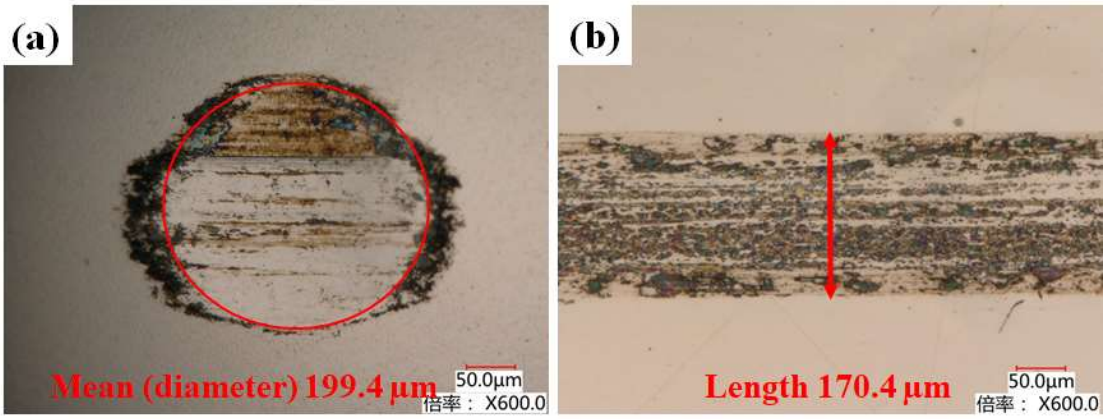

Fig. 4.36 Optical micrographs of wear scar (a) and wear track (b) on the ball and disc, respectively, for steel against nickel-plated steel after the friction test of 600 cycles at a normal load of 0.5 N.

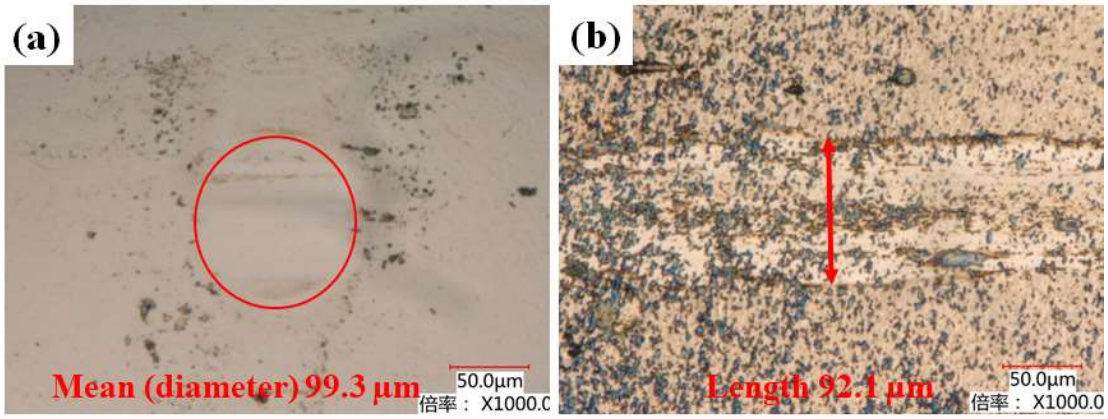

Fig. 4.37 Optical micrographs of wear scar (a) and wear track (b) on the ball and disc, respectively, for steel against multi-layer graphene-coated steel after the friction test of 600 cycles at a normal load of 0.5 N.

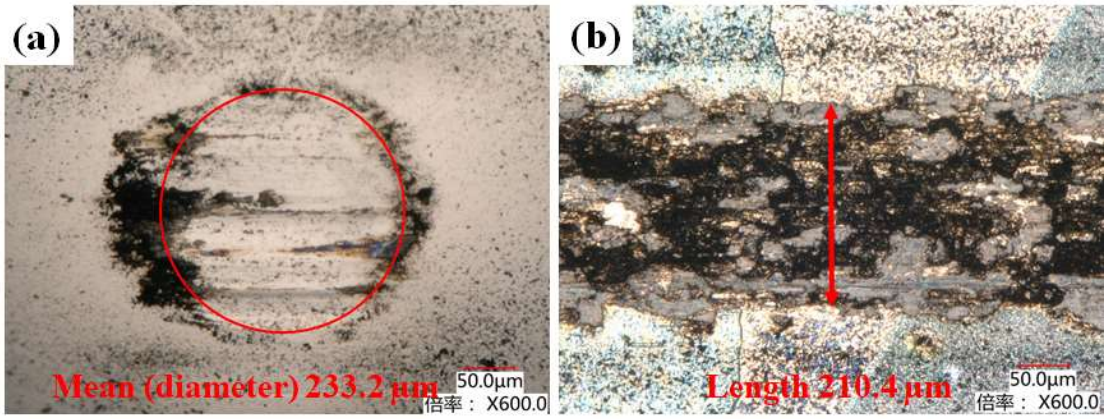

Fig. 4.38 Optical micrographs of wear scar (a) and wear track (b) on the ball and disc, respectively, for steel against multi-layer graphene-coated steel after the friction test of 600 cycles at a normal load of 1 N.

Figure 4.39 presents the wear scar diameters as a function of normal load for different combinations of tribo-pairs after the friction tests of 600 cycles at a normal load 0.5 N and a sliding speed of 0.01 m/s. The diameter of wear scar has been found to increase with increasing load for the balls tested against base as well as Ni-plated steel. The diameter of wear scar for the ball slid against base steel is found to increase from 0.16 mm to 0.31 mm, with the increase in load from 0.1 to 1 N, whereas the same for steel ball tested against nickel-plated steel disc has been found to increase from 0.15 to 0.28 mm. The wear scar diameter for steel ball tested against multi-layer graphene-coated steel disc has been observed to decrease with the increase in load from 0.1 to 0.5 N beyond which it is found to increase slightly for a load of 1 N as seen from Fig. 4.39. However, the diameter of the scar is significantly less in comparison to those observed for base steel and nickel-plated steel at each load, as evident from Fig. 4.39. The wear scar diameters are found to be 0.13, 0.12, 0.1 and 0.23 mm for loads of 0.1, 0.3, 0.5, and 1 N, respectively, for the ball slid against graphene-coated steel.

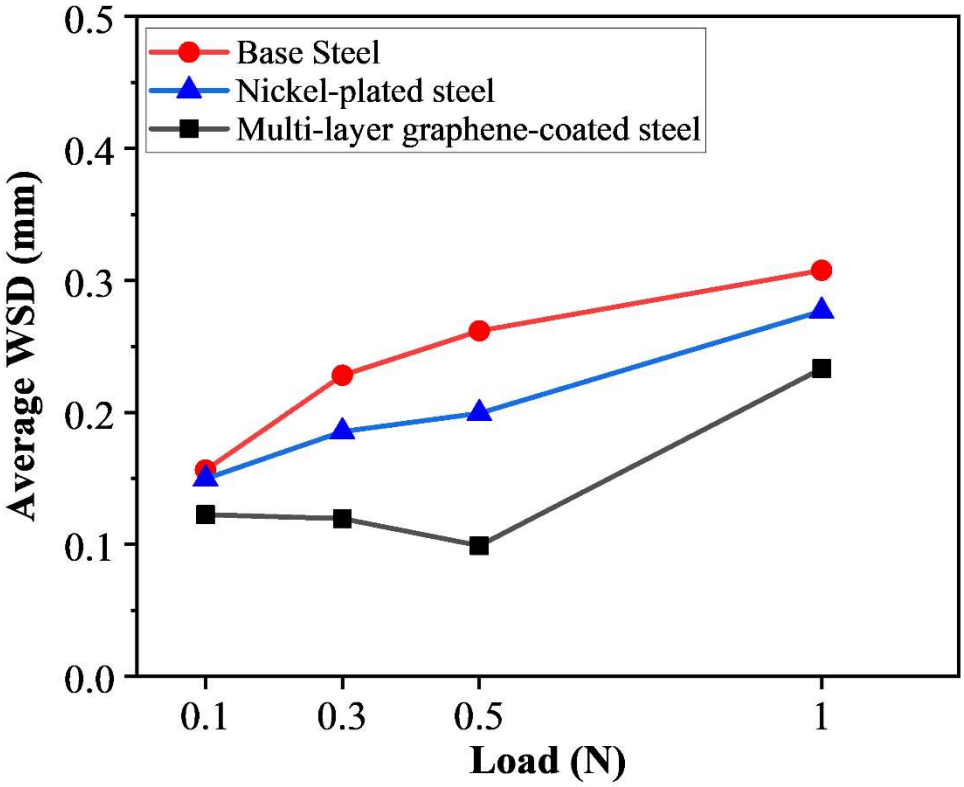

Fig. 4.39 Average wear scar diameter of the counterpart steel balls as a function of applied normal load after the friction tests.

Figure 4.40 depicts the ball wear volume, calculated on the basis of wear scar diameter, as a function of the normal load after friction tests of 600 cycles at a sliding speed of 0.01 m/s and the respective values are given in Table 4.7. The wear volume has been observed to increase with increasing load for the balls slid against base and Ni-plated steel, whereas the wear volume of the ball slid against graphene-coated steel is found to decrease with increasing load from 0.1 to 0.5 N followed by a slight increase for 1 N. The wear volumes of the balls used against base steel are the highest, whereas these are lowest for the balls slid against multi-layer graphene-coated steel at each load as evident from Fig. 4.40. One may also observe a significant decrease in wear volume by deposition of graphene coating on steel in comparison to both base as well as Ni-plated steel.

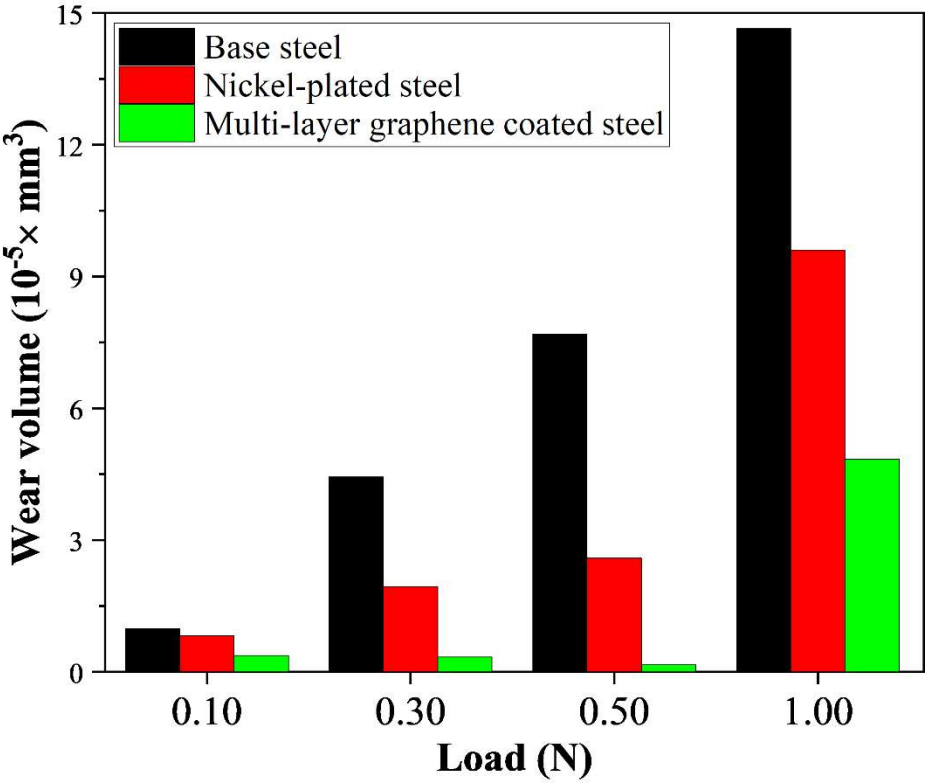

Fig. 4.40 Wear volume of the counterpart steel balls as a function of applied normal load after the friction tests.

Table 4.7 Ball wear volume of different friction pairs after the sliding tests of 600 cycles different normal loads.

Load (N)	**Wear volume (mm^3)**		
	Steel ball vs base steel	**Steel ball vs nickel-plated steel**	**Steel ball vs multi-layer graphene-coated steel**
0.1	0.98×10^{-5}	0.82×10^{-5}	0.37×10^{-5}
0.3	4.44×10^{-5}	1.94×10^{-5}	0.34×10^{-5}
0.5	7.69×10^{-5}	2.59×10^{-5}	0.16×10^{-5}
1	14.65×10^{-5}	9.61×10^{-5}	4.84×10^{-5}

Figures 4.41, 4.42, and 4.43 show SEM images and corresponding energy-dispersive spectra of the whole worn tracks on the base steel, nickel-plated steel, and multi-layer graphene-coated steel, respectively, after reciprocating sliding tests at a normal load of 0.5 N and sliding speed of 0.01 m/s. The worn surface of base steel given in Fig. 4.41 (a) shows fine scratches along the sliding direction, which appear to be covered by a layer of oxide probably of iron, as evidenced by the EDS spectrum, along with the presence of some wear debris particles. One may also observe the presence of voids and micro-cracks at few locations, which might have been caused by the detachment of layers. Figure 4.42 (a) clearly suggests the occurrence of adhesion on the worn surface of nickel-plated steel with more obvious. The surface is found to be covered by a relatively thick and well compacted glazed layer of nickel oxide, as indicated by the EDS spectrum. However, this layer appears to have been delaminated at few places leading to exposure of the underlying substrate pointing toward adhesion and delamination type of mechanism. Figure 4.43 (a) corresponding to worn surface of graphene-coated steel reveals the presence of a well-compacted layer containing graphene covering the most of the area of surface along with some deep scoring marks caused by the asperities of counterface. The presence of graphene, as a solid lubricant, might have reduced the adhesion and the abrasive wear appears to have dominated as evidenced from relatively deep tracks in Fig. 4.43 (a). The EDS spectrum analyses of the wear tracks shown in Figs 4.41 (b), 4.42 (b), and 4.43 (b) suggest a significant increase in carbon content for multi-layer graphene-coated steel, which appears in the form of a compacted layer over the surface. The elemental analysis also indicates the strong oxidation of steel (Fig. 4.41 (b)) and nickel-plated steel surfaces (Fig. 4.42 (b)), while multi-layer graphene-coated surface (Fig. 4.43 (b)) depicts the mild oxidation.

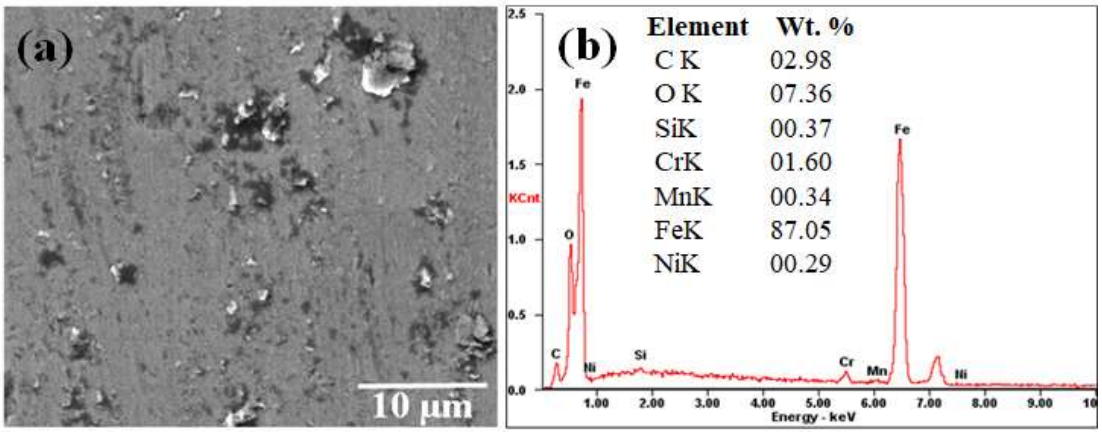

Fig. 4.41 SEM image and corresponding energy dispersive spectroscopy (EDS) analysis of wear track on the base steel disc after the friction test of 600 cycles at a normal load of 0.5 N.

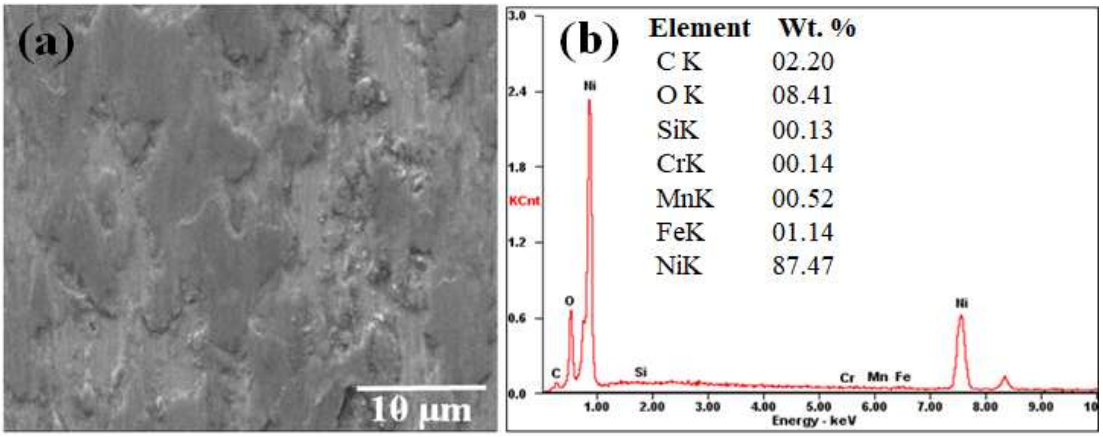

Fig. 4.42 SEM image and corresponding energy dispersive spectroscopy (EDS) analysis of wear track on the nickel-plated steel disc after the friction test of 600 cycles at a normal load of 0.5 N.

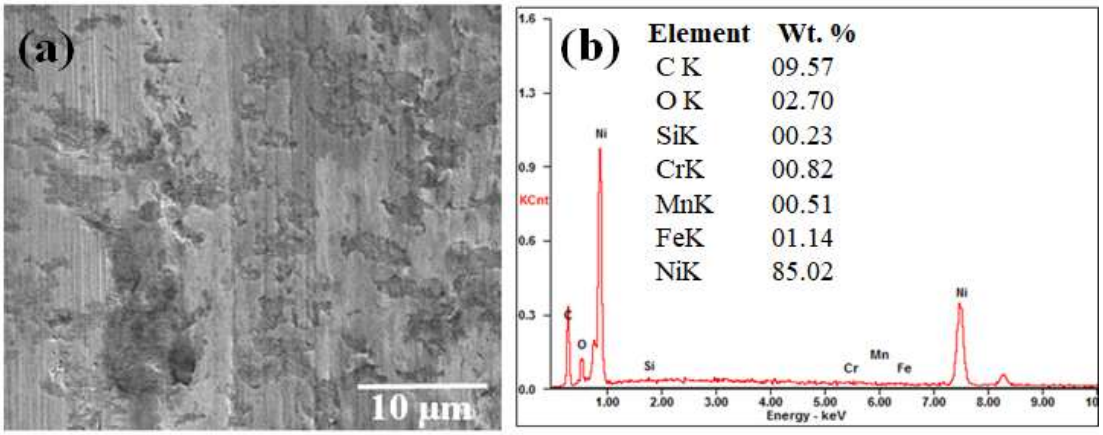

Fig. 4.43 SEM image and corresponding energy dispersive spectroscopy (EDS) analysis of wear track on the multi-layer graphene-coated steel disc after the friction test of 600 cycles at a normal load of 0.5 N.

The SEM images of the counterparts (balls) after the friction test at a normal load of 0.5 N are presented in Figs. 4.44 (a-c), whereas the worn surface of the ball after sliding under a normal load of 1 N is shown in Fig. 4.44 (d). A significant decrease in wear scar could be seen for multi-layer graphene-coated steel for friction test at a normal load of 0.5 N in comparison to both base steel and nickel-coated steel with no obvious loss of ball material. However, an increase in loss of ball material has been observed due to metal-to-metal contact brought about by the failure of the coating after 250 cycles, at a load of 1 N.

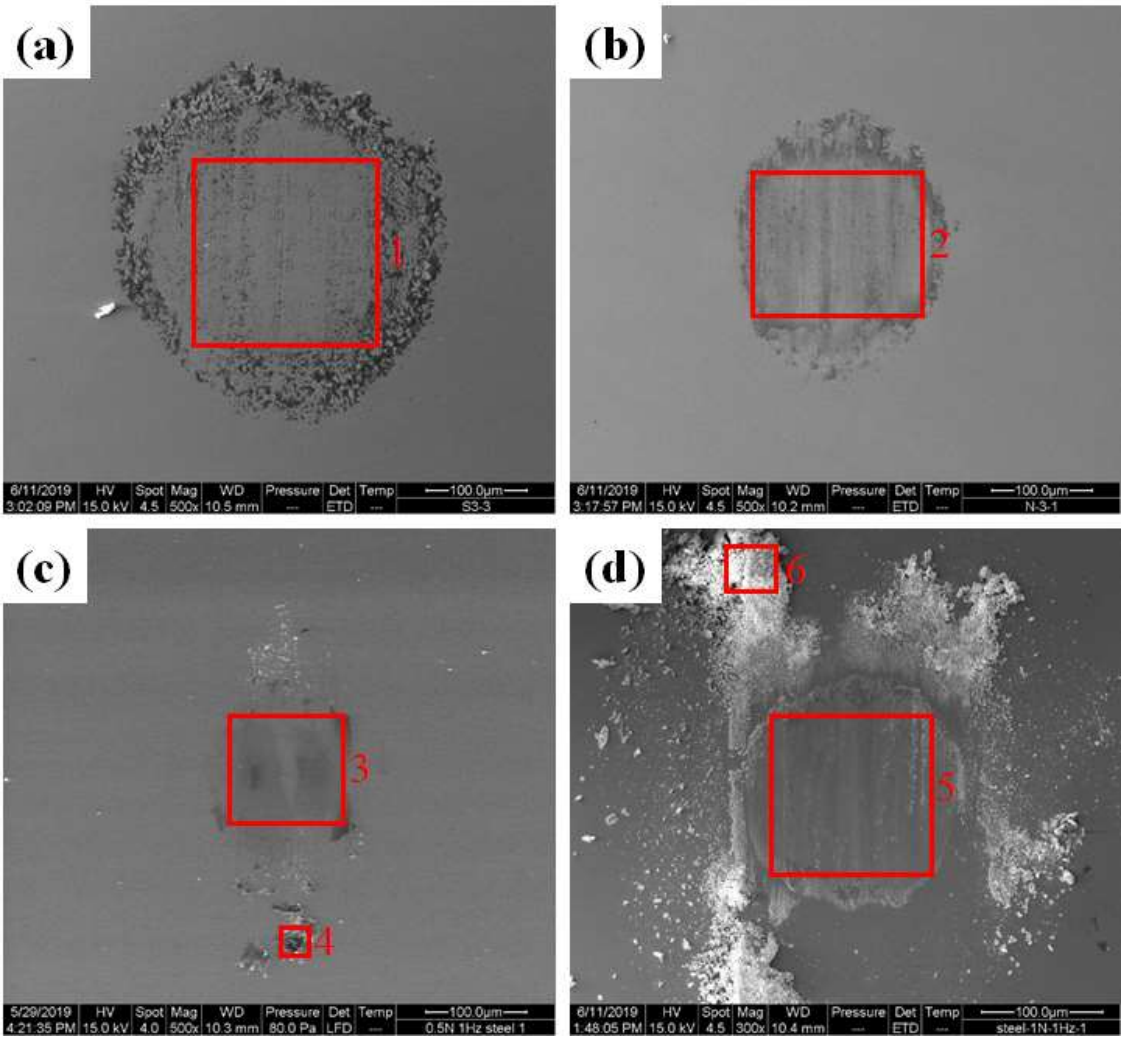

Fig. 4.44 SEM images of the worn counterpart surfaces (balls) slid against (a) base steel, (b) nickel-plated steel, (c, d) multi-layer graphene-coated steel after the friction tests of 600 cycles under the normal loads of (c) 0.5 N and (d) 1N.

Table 4.8 gives the chemical composition of different areas of wear scar (marked by squares in Fig. 4.44) as determined through EDS. The ball (blank) designation in Table 4.8 represents the chemical composition of the original ball. One may observe an increase in carbon percentage for the steel ball slid against multi-layer graphene-coated steel with minimum oxidation, as suggested by the data presented in Table 4.8.

Table 4.8 EDS analysis of the different areas of the ball, as mentioned in Fig. 4.44 after the friction tests of 600 cycles under a normal load of 0.5 N.

EDS area	**Chemical composition (wt. %)**						
	C	**O**	**Fe**	**Cr**	**Ni**	**Mn**	**Si**
Ball (Blank)	0.90	1.18	93.73	1.99	0.87	0.86	0.47
Point 1	1.80	2.52	92.62	1.71	0.38	0.65	0.32
Point 2	1.29	4.75	83.36	1.55	8.55	0.29	0.21
Point 3	2.80	1.43	90.44	2.10	1.59	1.21	0.43
Point 4	17.71	1.18	77.53	1.66	0.87	0.75	0.30
Point 5	1.38	3.63	86.13	1.93	4.93	1.51	0.49
Point 6	5.07	3.68	84.66	2.12	3.14	0.91	0.42

The worn surfaces of disc and ball have been subjected to Raman spectroscopy to confirm the existence of graphene on steel surface after the reciprocating dry sliding friction tests and to confirm the transfer of graphene to the counter surface,

i.e., ball. Figure 4.45 illustrates the Raman spectra of the worn surfaces of ball and disc after the friction tests of 600 cycles at a normal load of 0.5 N and a sliding speed of 0.01 m/s. All the three characteristics peaks (D, G, and 2D) are observed to be present on the surfaces of both ball and disc, as evident from Fig. 4.45. A sharp D peak for wear scar as well as for wear track can also be observed, and the I_D/I_G ratios for graphene for wear scar and wear track are found to be ~ 1.38 and ~ 1.20, respectively, which are a little higher than that of as-deposited optimised multi-layer graphene-coating on disc given in Fig. 4.11 indicating the incorporation of defects during the sliding test.

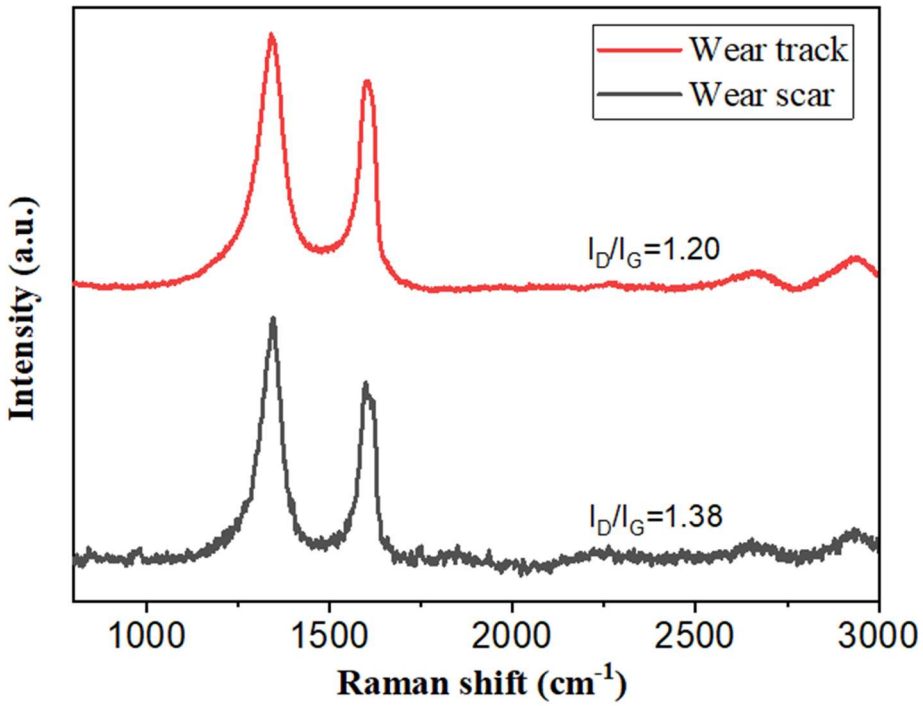

Fig. 4.45 Raman spectra of the wear track and wear scar after the friction test under 0.5 N load for multi-layer graphene-coated steel.

Further, the worn surface of the counterface ball has also been examined under transmission electron microscopy (TEM) to confirm the transfer of the graphene to the counter surface. Figures 4.46 (a, b) present the TEM images of wear scar of the ball

used against multi-layer graphene-coated disc after the friction test, which clearly reveals the presence of tribo-layer containing fragments of graphene and amorphous carbon. This tribo-layer is expected to protect the mating surfaces from direct metal-to-metal contact. The thickness of the transferred layer is found to be 5 ± 2 nm approximately, as evident from Figs. 4.46 (a, b). Figures 4.46 (c, d) present the TEM images of the wear track on the multi-layer coated-steel disc after the friction test. Similar to wear scar, the TEM images of wear track have also revealed the presence of tribo-layer even after friction tests consisting of fragments of graphene and amorphous carbon. The thickness of multi-layer graphene has been found to be 10 ± 2 nm, as evident from Figs. 4.46 (c, d).

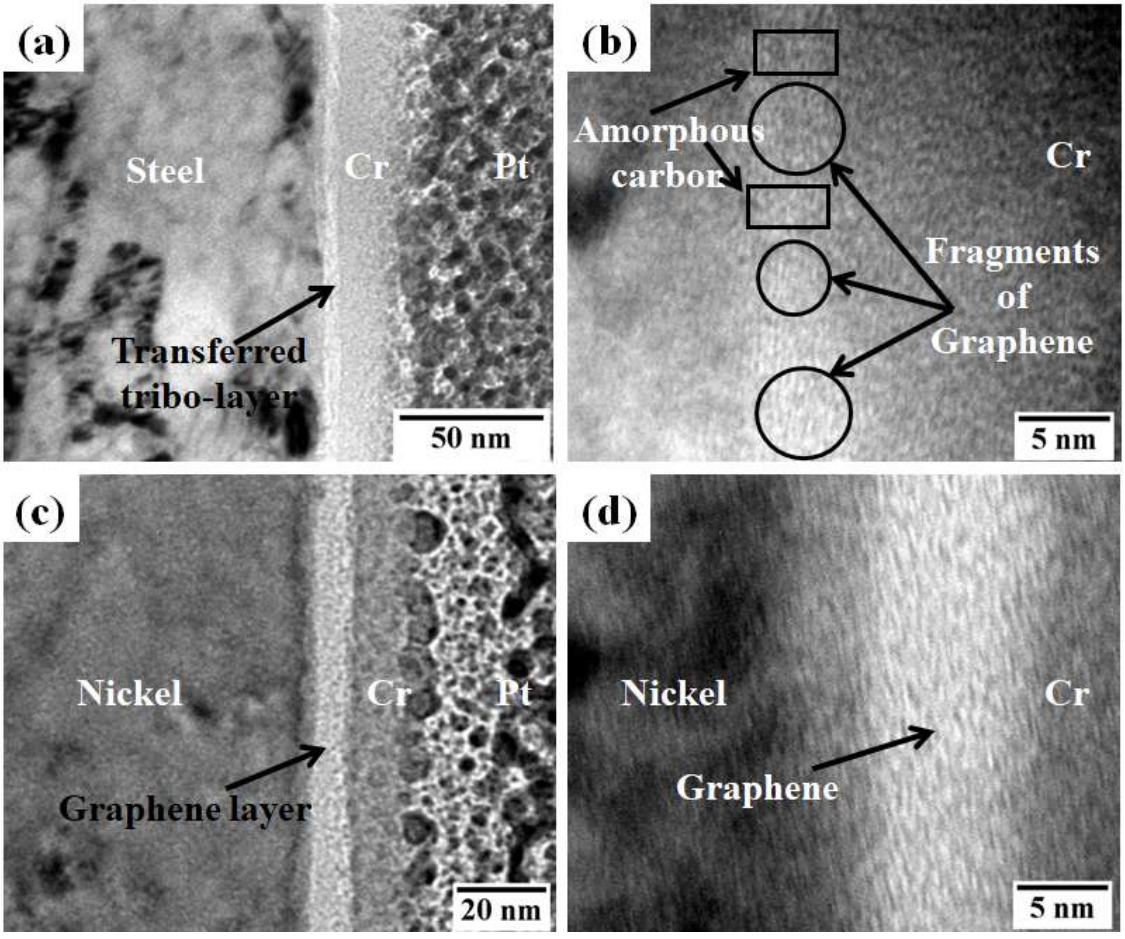

Fig. 4.46 Cross-sectional TEM images of wear scar (a, b) on the steel ball and wear track (c, d) on the multi-layer graphene-coated steel disc after the wear test under a normal load of 0.5 N.

4.2 DISCUSSION

The quality of graphene grown on a substrate depends on various parameters such as growth temperature, hydrocarbon flow rate, and reaction time, etc. It has been reported earlier (Weatherup et al., 2012) that the graphene can be grown on nickel at a lower temperature than that required for its growth on copper. Hence a nickel layer has been selected as a catalysing layer for the growth of graphene in the present study. The CVD growth of graphene on nickel-plated steel can be explained on the basis of the diffusion of carbon atoms into the electroplated nickel layer at high temperature, followed by segregation on the nickel surface during cooling. According to the phase diagrams, the solubility of carbon in nickel increases with increase in temperature (Lander et al., 1952; Baraton et al., 2011). A solid solution of nickel and carbon is formed beyond 500 ℃ due to the absorption of carbon atoms into the nickel layer. Since it is not possible to grow graphene with a precise and uniform layering throughout the surface using nickel as a transition metal, the synthesis of graphene has been observed in the form of patches of various thicknesses, as evident from Figs 4.4, 4.7, and 4.10.

Raman spectra of synthesised graphene at different growth temperatures, shown in Fig. 4.5 illustrate the presence of all the three main characteristics peaks (D, G, and 2D) of graphene which is in concurrence with the earlier studies reported by Ferrari et al., (2006), Peng et al., (2013) and Nanda et al., (2016). The D peak represents zone-boundary phonons, which can be identified at ~ 1350 cm^{-1} in defected graphite. The defect may be in the form of point defects, dislocation, bending and overlapping of layers, substitutional impurities, and carbon adatoms, etc. The G peak is representative of doubly degenerate phonon made of sp^2 carbon bonds and occurs at ~ 1580 cm^{-1}. The 2D peak, centred around ~ 2700 cm^{-1} is caused by the second-order of zone-boundary phonon and

is independent of the G peak as indicated by Ferrari et al. (2006) and Peng et al. (2013). A sharp D peak observed in Fig. 4.5 for a growth temperature of 650 ℃, suggests the presence of a significant number of defects in the synthesised graphene and the sharpness of D peak may be ascribed to the poor graphitisation at relatively low temperatures. A decrease in D peak intensity with an increase in growth temperature, as seen in Fig. 4.5 reflects an improvement in the quality of graphene with increasing temperature, which may be attributed to better graphitisation at relatively higher temperatures. The presence of two more weak peaks at ~ 2460 cm^{-1} (G^*) and ~ 2944 cm^{-1} (D+D') may be credited to the inter-valley double resonant Raman process and the combination of D and G peaks, respectively, as observed earlier also by John et al., (2011).

The I_D/I_G ratio has been used to evaluate the quality of graphene. Generally, the lower the I_D/I_G ratio, the higher the quality of graphene. The I_D/I_G ratio has been found to increase with increasing temperature till 850 ℃ as evident from Fig.4.6, which reflects an improvement in the quality of graphene in the light of discussion mentioned above. The I_D/I_G ratio is significantly lower for a growth temperature higher than 850 ℃, which suggests that the synthesis of high-quality graphene at higher temperatures. The value of I_{2D}/I_G ratio is an indicator of the number of graphene layers. It has been reported that I_{2D}/I_G is ~ 1 for a bi-layer graphene, whereas for monolayer graphene, I_{2D}/I_G is usually higher and the number of layers increases with decreasing I_{2D}/I_G ratio (Umair, 2013; Lin et al., 2015). The I_{2D}/I_G ratios (< 1) observed in the current study suggest that the steel surface is covered by multi-layer graphene. Since the lowest I_D/I_G and the highest I_{2D}/I_G ratios have been observed for a growth temperature of 850 ℃; hence, this temperature has been chosen as optimum temperature to further analyse the effect of acetylene flow rate and reaction time on the growth of graphene.

An increase in the acetylene flow rate causes the suppression of 2D and G peak intensities and strengthens the D peak, as seen from Fig. 4.8, which may be attributed to the presence of sp^3 carbon atoms simultaneously with sp^2 carbon atoms after precipitation. However, a decrease in the 2D peak with an increased flow rate of acetylene may be due to the availability of more and more carbon atoms that get dissolved into nickel-plated steel. These carbon atoms then precipitated over the surface during cooling and resulted in increasing the number of graphene layers. A decreasing I_{2D}/I_G ratio, with an increase in acetylene flow rate as depicted from Fig. 4.9 suggests an increase in the number of layers. The I_D/I_G ratios have been found to lie under 0.05 for each flow rate, which shows that low defect graphene can be grown at all acetylene flow rates which has earlier been reported by Regmi et al., (2012). Since the maximum I_{2D}/I_G ratio and the minimum I_D/I_G have been observed for 6 sccm acetylene flow rate, it may be concluded that the best quality graphene can be grown under a low acetylene flow rate, i.e., 6 sccm at a growth temperature of 850 ℃.

Raman spectra given in Fig. 4.11 corresponding to reaction times of 10 and 20 min reveal the presence of all the three characteristics peaks with more intense G and 2D, which confirms that the graphene is of high quality for both reaction times. A slight increase in I_{2D}/I_G ratio observed for 10 min in comparison to 20 min points toward a reduction in the number of graphene layers for shorter reaction time. Hence, one may conclude that comparatively thinner graphene films can be synthesised at shorter reaction time. A similar finding has also been reported earlier by Guo and Zhang (2016) for the growth of graphene on nickel substrates by CVD. However, a shorter growth time is also preferred because too long growth time may expose the crystals to etching as indicated by Chae et al. (2009) and Papon et al. (2009).

A broad survey XPS spectrum of as-deposited multi-layer graphene illustrated in Fig. 4.13 has shown an intense peak at 284.6 eV, corresponding to C_{1s} (~ 92 at. %). Two other low-intensity peaks observed at 532 eV and 854 eV represent O_{1s} (~ 7.4 at. %) and Ni_{2p} (~ 0.6 at. %), respectively. The O_{1s} peak refers to molecular oxygen (O_2) that might have originated from the atmospheric air. The de-convolution of the C_{1s} spectrum of multi-layer graphene using Voigt approximation has shown a main peak at 284.6 eV and three other peaks centred at 285.9, 287.7, and 289 eV, respectively. The peak at 284.6 eV could be assigned to C=C and stands for sp^2-hybridised graphite-like carbon atoms. The peak at 285.9 eV represents the presence of the sp^3-hybridised amorphous carbon atoms whereas remaining two peaks at 287.7 eV and 289 eV may be attributed to C=O (ketone, aldehyde) and O-C=O (ester, acid, carboxylic) groups, respectively (Wang et al., 2009). On the basis of the results and discussion presented above, one may conclude that multi-layer graphene can be successfully synthesised using low-pressure CVD with few-oxygen containing functional groups on the surface of nickel-plated steel. TEM image depicted in Fig. 4.14 (a) confirms the layered structure of graphene, whereas Fig. 4.14 (b) suggests that the graphene layers stacked over each other, constituting thus, a multi-layer graphene.

The variation of coefficient of friction as a function of sliding cycles for different tribo-pairs, namely steel vs base steel, steel vs nickel-plated steel, steel vs multi-layer graphene-coated steel under unidirectional sliding given in Fig. 4.15, represents an unstable and fluctuating trend for steel ball against base steel and steel ball against nickel-plated steel tribo-pairs. When a test specimen is under dry sliding at relatively lower loads, frictional heating helps atmospheric oxidation over the sliding surface, the oxide layer gets removed by repeated, and multiple contacts and the wear debris of oxide particles is generated. The wear debris gets trapped between sliding surfaces and is compacted into a layer. The continuing process of removal of this layer and its

reformation results in the fluctuation in the coefficient of friction. The other contribution to fluctuation may come from the variation in the contact when the sample and the counterface are evolving to develop a better surface conformity due to smoothening of asperities. For the initial sliding of 800 cycles, the coefficient of friction (~ 0.89) is highest for steel against base steel. The electroplating of nickel over steel disc causes a reduction in the coefficient of friction to a value of ~ 0.66, as seen from Fig. 4.15. However, the variation of steel ball-graphene coated steel tribo-pair is quite smooth and a significant reduction in coefficient of friction is observed, which may be explained by the lubricating effect of graphene which provides an easy shearing film at the interface. The average coefficient of friction of ~ 0.15 is achieved throughout the friction test of 800 cycles, as evident from Fig. 4.15. The higher coefficient of friction observed for steel against base steel may also be explained on the basis of SEM micrographs of the worn surfaces of the disc given in Fig. 4.20 (a), which presents a deeply torn surface with scoring marks along the direction of sliding indicating the occurrence of direct metal-to-metal contact due to increased asperity-asperity interactions. A rough morphology of counterface ball surface slid against base steel and presented in Fig. 4.23 (a), also suggests relatively higher friction for steel ball-base steel tribo-pair. This may also explain a higher wear volume and wear rate for the ball slid against base steel, as seen from Fig. 4.19 and Table 4.4. A decrease in the coefficient of friction for the steel against nickel-plated steel may be due to the presence of a smooth layer over the worn surface of nickel-plated steel given in Fig. 4.21 (a), which inhibits direct contact between the ball and the steel disc, resulting in slightly reduced friction as well as wear, as seen from Figs. 4.15 and 4.19. The SEM micrographs of the worn surface of the corresponding counter ball given in Fig. 4.23 (b) also reveals a relatively smoother surface in comparison to that observed for the ball slid against base steel (Fig. 4.23 (a)) pointing towards a diminished metal-to-metal contact. A

significant decrease in coefficient of friction for steel ball-multi-layer graphene-coated steel tribo-pair observed in Fig. 4.15 could be attributed to the effectiveness of graphene in providing lubrication, which has also been reported by Restuccia and Righi (2016). In the beginning of the test, graphene-to-metal contact occurs, but as the sliding progresses, the graphene gets transferred to the ball surface leading to a contact between the graphene-coated steel disc and graphene transferred to the ball, which provides an easy shearing capability between the mating bodies and results in a reduced coefficient of friction, wear volume and wear rate, as seen from Figs. 4.15 and 4.19, respectively. The presence of graphene on the worn surface of the disc as well as on the worn surface of the ball has been confirmed by their respective Raman spectra illustrated in Figs. 4.24 (b and d). The increase in carbon contents for both the ball and the multi-layer graphene-coated steel after sliding tests, as indicated by EDS analysis given in Table 4.5, also suggests the presence of graphene in the form of increase in carbon contents. One may observe very fine scoring marks with no visible signs of adhesion on the worn surface of graphene-coated steel shown in Fig. 4.22 (a) and a smooth worn surface of ball depicted in Fig. 4.23 (c). This may also explain a significant reduction in the coefficient of friction and wear volume/rate for steel-graphene coated steel tribo-pair.

The friction and wear behaviour have also been examined for long-duration sliding tests of 5600 cycles. A fluctuating trend of variation of coefficient of friction with the number of cycles depicted in Fig. 4.25, may again be explained on the basis of the formation-removal-reformation of the oxide layer, entrapment of wear debris between the sliding bodies and evolution of better surface compatibility, as explained earlier. The coefficient of friction of steel against nickel-plated steel is lower than steel-base steel tribo-pair up to 1000 cycles and increases after that, as evident from Fig. 4.25. This may be attributed to the initiation of steel-steel contact after 1000 cycles due to loss of

electroplated nickel layer during the sliding tests. The smooth and stable frictional behaviour for the steel against multi-layer graphene-coated steel, as seen in Fig. 4.25 reflects the lubricious effects of graphene coating. However, an increase in the average value of the coefficient of friction (~ 0.18) for long-duration sliding in comparison to short duration sliding (~ 0.15) may be due to the loss of graphene coating with time. The severe damage of the worn surfaces as seen from optical images (Figs.4.26 (a and b)) and SEM images (Figs. 30 (a and b)) indicates the occurrence of direct steel-to-steel contact, which might have resulted in increased wear volume and wear rate for steel-base steel tribo-system as evident from Fig. 4.29. A relatively smoother surface as observed for steel-nickel plated steel presented in Figs. 30 (c and d) shows the presence of compacted layers on the worn surface probably of nickel oxide and thus avoiding the steel-to-steel contact to some extent. The worn surface of the steel ball slid against multi-layer graphene coating given in Fig. 4.30 (e and f) presents a relatively smooth surface, which might have been due to establishment of contact between the graphene on the coated surface and the graphene transferred to the ball, which is confirmed by the Raman spectrum depicted in Fig. 4.31. The avoidance of asperity-asperity contact between the mating bodies due to this graphene-graphene contact might have resulted in a reduced wear volume/rate for the ball slid against graphene-coated steel, as evident in Fig. 4.29.

The variation of coefficients of friction as a function of sliding cycles for different tribo-pairs, namely steel vs base steel, steel vs nickel-plated steel, steel vs multi-layer graphene-coated steel under reciprocating sliding has been shown in Fig. 4.32. The steel against base steel has large fluctuations and a high coefficient of friction throughout the friction test, which may be ascribed to direct metal-to-metal contact as discussed earlier and can be explained on the basis of SEM micrographs of worn surfaces of the disc and ball given in Figs. 4.41 (a) and 4.44 (a), which present relatively rough surfaces with fine scratches along the sliding direction. A slight decrease in coefficient of friction

for the steel against nickel-plated steel, as seen in Fig. 4.32, may be attributed to the formation of a well compacted and thick glaze layer of nickel oxide on the disc surface, as evident in Fig. 4.42 (a), which contributes to a slight reduction in the coefficient of friction between the friction surfaces (Torgerson et al., 2018). The significant reduction in friction for multi-layer graphene-coated steel observed in Fig. 4.32 reflects the solid lubrication effect of graphene, which may be explained by the SEM micrographs shown in Figs. 4.43 (a) and 4.44 (c). Multi-layer graphene coating on the disc surfaces has reduced the plastic deformation as well as adhesion to a great extent, and mainly, the abrasive wear has been observed to occur at the tribo-pair interfaces, as evident from Figs. 4.43 (a) and 4.44 (c). The multi-layer graphene from the disc surface has been found to transfer partially on the surface of the steel ball during the sliding test, and thus initiating the graphene-graphene contact during sliding, which has also been confirmed by Raman spectra (Fig. 4.45) and TEM images (Fig. 4.46). The multi-layer graphene coating over steel provides the protection to the underlying substrate by avoiding the direct metal-to-metal contact and utilises the property of low interlayer shearing strength of graphene in affecting a reduction in friction. The EDS analysis of the worn surface of the counter ball has also shown the increased carbon (Table 4.8) indicating the transfer of carbon on the ball, which originates from the transfer of graphene on the ball surface during sliding. Hence, low interlayer shear strength between the graphene-graphene interfaces is a reason behind the improved anti-friction behaviour.

The increasing trends of variation of average coefficient of friction with normal load seen in Fig. 4.34 for the steel against base steel and steel against nickel-plated steel may be due to enhanced possibility of direct metal-to-metal contact caused by increasing contact stress and penetration of asperities at increasing normal load. This may also explain an increased wear volume with increasing load for the ball slid against base steel as illustrated in Fig. 4.40. A lower coefficient of friction for steel-nickel plated tribo-

pair may be attributed to the presence of the nickel layer, which is able to inhibit direct contact between ball and substrate steel to a certain extent. However, with increasing load either there occurs a loss of nickel-coating, or the asperities of counterface are able to penetrate this layer. Both of these conditions lead to an increase in direct contact between the mating bodies and result in an increase in coefficient of friction as well as wear volume, as seen in Figs. 4.34 and 4.40, respectively. However, a significant reduction in the coefficient of friction for steel vs graphene-coated steel tribo-pair in comparison to other tribo-pairs, as observed in Fig. 4.34 may be attributed to the lubricious effect of graphene, which has also been reported earlier by Restuccia and Righi (2016). A decrease in coefficient of friction with increasing load from 0.1 to 0.5 N for steel-graphene coated steel tribo-system as seen from Fig. 4.34 may be attributed to homogenisation and smoothening of graphene coatings with an increase in load, as indicated earlier also by Xu et al. (2018). This may also explain a decrease in wear volume for the ball slid against graphene coated steel, as observed in Fig. 4.40. An increase in the coefficient of friction beyond 0.5 N (Fig. 4.34) is possibly due to the failure of graphene coating after ~ 250 cycles as evident from Fig. 4.38 (b), which exposes the underlying substrate and results in direct contact between the steel ball and substrate. This may also be responsible for the sudden increase in the coefficient of friction, as observed in Fig. 4.33 as well as the wear volume, as evident from Fig. 4.40. The lowest wear volume for multi-layer graphene-coated steel at every load in comparison to that for base steel and nickel-plated steel observed in Fig. 4.40 suggests the positive lubrication effect of graphene at each load. TEM images of wear scar on ball and corresponding wear track on multi-layer graphene-coated disc presented in Figs. 4.46 (a and b) indicate a transfer of graphene coating, consisting of fragments of graphene and amorphous carbon, to the counterface ball. This might have resulted in the interaction between transferred graphene and graphene-coated steel rather than graphene against steel, leading to a decrease in both the coefficient of friction and wear volume.

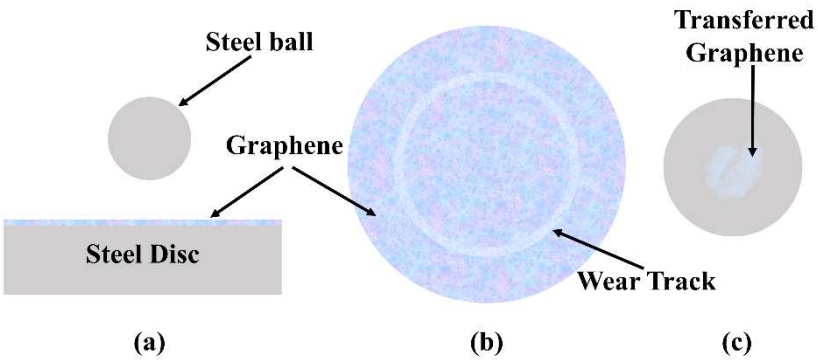

Fig. 4.47 Graphical representation of wear mechanisms of graphene coatings (a) initial graphene-coated steel and steel ball, (b) wear track and (c) transferred graphene on steel ball after the friction tests.

Based on the examination of SEM micrographs of worn surfaces and discussion presented above, it may be inferred that the wear mechanisms associated with steel-base steel is a mixture of adhesion, abrasion and wear induced oxidation. The wear mechanisms for steel-nickel plated steel is adhesion and mild oxidation as suggested by the SEM morphologies of the worn surfaces of the disc. However, mild abrasion is the dominating mechanism of wear for steel-graphene coated steel tribo-pair as suggested by the fine scoring marks on the worn surface. The wear mechanism has been presented graphically in Fig. 4.47. One may observe that directly grown multi-layer graphene retains itself firmly on the surface of the disc and provides an effective cover to the underlying substrate against direct contact between mating bodies. On the other hand, a partial transfer of graphene to the counterface (ball) during the sliding process also provides a protective layer of graphene over the counterface of steel, which results in contact between the transferred and coated graphene. Both of these conditions help in preventing the direct contact between mating bodies tribo-pairs and result in a significant reduction in both the coefficient of friction and the wear. Overall, multi-layer graphene-coating on steel has the potential of significantly enhancing the tribological performance of self-mated steel pair.